MICROBOONE-NOTE-1045-PUB

Version 1.4

First Muon-Neutrino Charged-Current Inclusive Differential Cross Section Measurement for MicroBooNE Run 1 Data

The MicroBooNE Collaboration

May 29, 2018

Abstract

This note presents MicroBooNE's first ν_μ charged-current (CC) inclusive measurement using 6 months of Run 1 data ($\sim 1.6 \times 10^{20}$ POT). The measurement is presented as a function of reconstructed muon kinematics, including a first assessment of systematic uncertainties.

The signal topology for a ν_μ CC inclusive measurement is the presence of a neutrino-induced muon track with or without other accompanying particles. It is therefore the most inclusive cross section measurement that can be made, and due to the very clear signal definition allows straight-forward comparisons to theory models and other experiments. Additionally, this analysis selection can be used for more exclusive-channel cross section measurements, and be used to further develop reconstruction and event selection techniques. The note also discusses the techniques developed to distinguish neutrino-induced from cosmic muons for a sample with full angular coverage.

Contents

1 Introduction

This note presents MicroBooNE's first ν_μ charged-current (CC) inclusive measurement using six months of Run 1 data: $\sim 1.6 \times 10^{20}$ protons-on-target (POT). The signal topology for a ν_μ CC inclusive measurement is the presence and identification of a neutrino-induced muon with or without other accompanying particles. It is therefore the most inclusive cross section measurement we can make, and due to the very clear signal definition allows straight-forward comparisons to theory models and other experiments.

Most of our knowledge of neutrino cross sections around the ~ 1 GeV energy range comes from experiments with light nuclear targets. Current and future experiments employ heavier nuclei (e.g. iron, water or argon) as a target material. Nuclear effects that complicate the understanding of neutrino scattering play an important role. In addition to the absorption of the W boson by a single nucleon which is knocked out leading to the so called $1p1h$ excitation, coupling to nucleons belonging to correlated pairs (short-range nucleon-nucleon correlations) and to two-nucleon currents arising from meson exchange (MEC) must also be considered. This leads to the excitation of multi-nucleon or $2p2h$ excitations. The CC inclusive

channel is somewhat sensitive to these effects through measuring the overall cross section and studying muon kinematic distributions.

Previous experiments like SciBooNE, NOMAD, MINOS, ArgoNeuT, MINERvA, and T2K have also measured the CC inclusive cross section. ArgoNeuT [1, 2] and the T2K on-axis detector INGRID [3, 4] published flux-integrated measurements. ArgoNeuT is the only experiment that has published cross sections for neutrino-argon scattering to date. SciBooNE [5], NOMAD [6], MINOS [7], and MINERvA [8, 9] all published CC inclusive cross sections as a function of a reconstructed neutrino energy.

Besides the physics itself, this CC inclusive measurement has huge value for the development of reconstruction and selection tools in MicroBooNE. Since the detector is located on the surface, it is constantly pierced by cosmic rays, which constitute the main background when looking for neutrino-induced muon tracks. This note describes the techniques developed to distinguish neutrino-induced particles from cosmic muons for a sample with full angular coverage. The final sample will be used as pre-selection for more exclusive channels in the near future.

2 Detector

MicroBooNE is a Liquid Argon Time Projection Chamber (LArTPC) detector [10] and the heavy Argon target, compared to previous experiments, will allow to better study nuclear effects. In MicroBooNE, charged particles traversing a volume of highly-purified liquid Argon leave trails of ionisation electrons in their wake and also create prompt vacuum ultraviolet scintillation photons. Ionization electrons are detected by a system of anode wires in three planes and scintillation photons are observed by a 32 photo-multipliers located behind them.

The MicroBooNE detector is located in the Booster Neutrino Beam (BNB) at Fermilab, which is producing neutrinos between a few tens of MeV to 2 GeV.

3 Data Samples, Simulation, and Event Reconstruction

3.1 Data Samples

MicroBooNE began recording neutrino interactions in October of 2015. The experiment completed the commissioning of the trigger system (see Section 3.3.1) in February 2016. The dataset used in this analysis ranges from February to July 2016.

Two different data streams are utilised in this note:

On-beam data: Taken only when the arrival of a beam spill from the BNB is expected.

Off-beam data: Taken during periods when no beam was received and used for a data-driven measurement of cosmic backgrounds. It is taken with the same conditions as on-beam data.

Data quality criteria include successful operation of all detector systems, detector stability in high-level parameters relevant for this analysis and beam quality. After these requirements, the on-beam data available for this analysis correspond to 1.627×10^{20} POT.

3.2 Simulation

The simulation chain for beam induced neutrino interactions in MicroBooNE consists of the following steps:

Flux simulation: The simulation of the neutrino flux produced by the BNB beam line is based on GEANT4 [11] simulations. It includes a full simulation of the production of hadrons by the 8 GeV primary proton beam interacting with the BNB target and the propagation of those hadrons through the target, magnetic horns, and along the decay pipe [12, 13].

Simulation of neutrino interactions: The generation of neutrino interactions in the MicroBooNE detector is performed using the GENIE MC simulator [14], `v2_12_2`. GENIE simulates the primary interaction inside the nucleus, the production of all final-state particles in the nucleus (hadronisation), and the transport and rescattering of the final-state particles through the nucleus (intranuclear transport). The baseline GENIE simulation is referred to in this note as "Default GENIE + Emp. MEC", and is based on the default GENIE model set, including MEC events. An alternative set of models we are comparing to in this note is referred to as "GENIE Alternative". Details to both versions are listed in Table 1. "Default GENIE + Emp. MEC" is the GENIE default model set choice, while GENIE Alternative represents a theoretically driven set of models for MicroBooNE energies.

Overlay of cosmic backgrounds: Since MicroBooNE is located on the surface and the duration of an event is determined by the typical drift time of 2.3 ms, each neutrino beam interaction is overlaid with multiple cosmic rays. Cosmic rays are simulated with CORSIKA [15], version `7.4003`.

Detector simulation: The simulation of the MicroBooNE detector is based on GEANT4 and includes particle propagation, electron drifting to the wire planes, as well as scintillation light to the photomultipliers (PMTs).

Model element	Default GENIE + Emp. MEC	GENIE Alternative
Nuclear Model	Bodek-Ritchie Fermi Gas [17]	Local Fermi Gas [18, 19]
Quasi-elastic	Llewellyn-Smith [20]	Nieves [18, 19]
Meson-exchange Currents	Empirical [21]	Nieves [18, 19]
Resonant	Rein-Seghal [22]	Berger-Seghal [23]
Coherent	Rein-Seghal [22]	Berger-Seghal [23]
FSI	hA [24]	hA2014 [24]

Table 1: The two GENIE model sets used in this analysis.

All simulation is carried out within the `LArSoft` framework [16].

3.3 Event Reconstruction

3.3.1 Triggering and optical reconstruction

Every recorded event in the on-beam stream corresponds to a BNB neutrino spill, although the majority of the spills do not produce a neutrino interaction in the detector. In order to reduce the amount of recorded data, not every spill is saved. A software trigger is applied which quickly determines if the event contains coincident activity in the TPC, based on light deposition in the optical detectors. This trigger looks at light activity on the PMTs in time-coincidence with the 1.6 μs beam-spill reaching the detector. This activity may be caused by a neutrino interaction, coincident cosmic activity, or some other coincident sources. The trigger reduces the data rate by a factor 20. The signal efficiency loss through the trigger condition is negligibly small for this analysis, and the trigger cut is in any case superseded by a much higher minimum optical light deposition analysis cut later. The subsequent optical reconstruction collects raw waveforms recorded by individual PMTs and combines them to reconstructed flashes, which represent optical activity in time across several PMTs, usually caused by a single interaction in the TPC. These reconstructed flashes are then used for the downstream analysis.

3.3.2 TPC Reconstruction

The input data to the TPC reconstruction consists of waveforms in the drift time of charge induced or deposited on the sense wires. These waveforms first pass through a filtering algorithm in order to reduce the noise introduced by the electronics and through pick-up on the sense wires themselves [25].

After noise filtering, they are passed to the hit finding algorithm which identifies candidate peaks in the waveforms and fits them with a Gaussian shape in order to

obtain a "hit" representing the charge deposited on that wire by the incident track. Hits are represented as objects with a peak time and width and serve as the basic input to the reconstruction algorithms.

Hits are then grouped into clusters. The purpose of the cluster algorithm is to group hits which correspond to the same particle signature, i.e. a track or shower.

This analysis utilises the Pandora multi-algorithm pattern recognition framework, which handles the clustering of hits, as well as the reconstruction of 3D objects [26].

The output of the Pandora multi-algorithm pattern recognition is structured in "PFParticles" (PF stands for Particle Flow) reconstructed particles, each one corresponding to a distinct track or shower, and their hierarchy, which identifies parent-daughter relationships and describes the particle flow in the observed interactions. A neutrino PFParticle is created as part of the hierarchy and forms the primary parent particle for a neutrino interaction.

LArTPCs provide excellent calorimetric information. Calorimetry can be used to make a measurement of a particle energy deposition, useful to understand the particle type (PID). Calorimetry is used in this analysis to identify stopping cosmic background muons, and to distinguish muon candidate tracks from proton candidate tracks. The analysis uses a reconstructed truncated mean charge deposition along the length of the track dQ/dx, displayed in Fig. 1. The truncated mean is used instead of the mean or median of the full distribution because it is less sensitive to fluctuations. The variable is obtained per plane, with only the collection plane being used in this analysis. The calibration of the variable is performed in simulation and data using cosmic muons. The data and MC entries at $dQ/dx \sim 0$ are due to tracks aligned with the drift direction. In this case all of the charge arrives on very few collection plane wires, and the hit reconstruction tends to assign this large charge deposition to many hits. This leads to charge being missed "between" the fitted hits.

3.3.3 Cosmic Removal

MicroBooNE is a surface detector and is therefore constantly pierced by cosmic rays (CR). The removal of cosmic rays is fundamental for any physics analysis and is part of the reconstruction flow.

Immediately after hit reconstruction, reconstructed hits are passed to the Pandora software that performs pattern recognition. Pandora is run in two different modes [26]:

- `PandoraCosmic`, optimised for the reconstruction of cosmic rays and their daughter delta rays;
- `PandoraNu`, optimised for the reconstruction of neutrino interactions.

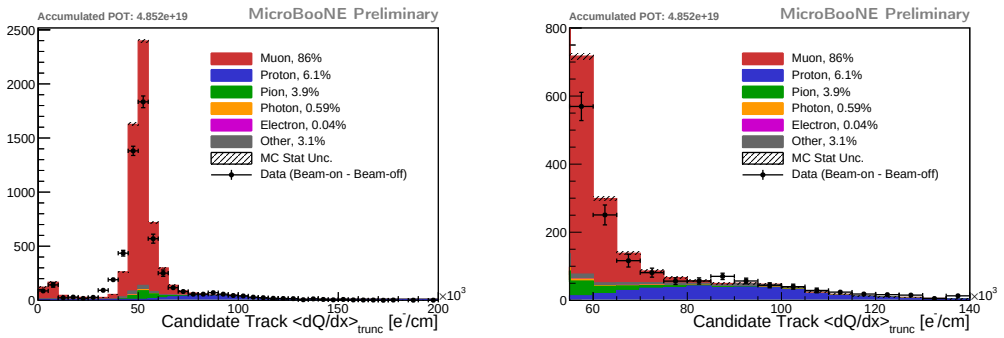

(a)

Figure 1: Distributions of the truncated mean dQ/dx for the muon candidate track. Black points are data points. The coloured histograms shows the MC (stacked). The right plot is an enlargement of the left one, showing that a proton track is selected as muon candidate for higher values of dQ/dx.

Pandora is first run in `PandoraCosmic` mode. The reconstructed tracks are then analysed by a series of algorithms that try to identify cosmic rays. The cosmic taggers are:

Geometrical Tagging of through-going tracks, which are both entering and exiting the detector volume.

Optical Tagging of cosmic rays whose predicted light profile is not compatible with the beam spill reconstructed flash.

Anode- or Cathode-piercing If tracks are crossing the anode or cathode, their start time can be easily estimated and compared to the beam spill time. Tracks incompatible with the arrival time of the beam are tagged.

Stopping muons Stopping muons are a challenging background since they can fake a ν_μ CC neutrino interaction starting inside the detector. They are tagged if a Michel electron or Bragg peak can be identified in the energy loss profile of the track, or if the pattern of multiple Coulomb scattering (MCS) [27] indicates a direction of the track that is consistent with an entering and stopping particle. The MCS algorithm decides on the direction of the particle by fitting both track direction hypotheses and comparing the log-likelihood values of the fit as shown in Fig. 2. A cut is applied so that tracks with $\Delta LL < -5$ are rejected. An enlargement around this cut value is shown in Fig. 2b showing good data/MC agreement.

Hits related to tagged cosmics are removed and the subset of hits remaining is passed to the Pandora framework, which is then run in `PandoraNu` mode.

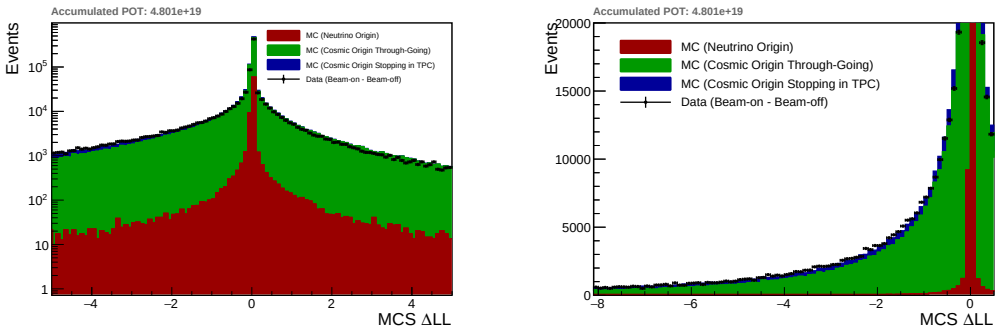

(a) (b)

Figure 2: The difference between the MCS log-likelihood in the forward and backward direction applied to all reconstructed tracks. If the track is entering the TPC from outside, the expected value of ΔLL is negative. The plots are POT normalised. The left plot is in logarithmic scale. The right plot is enlarged in the negative region, where there is the majority of stopping muons (blue histogram).

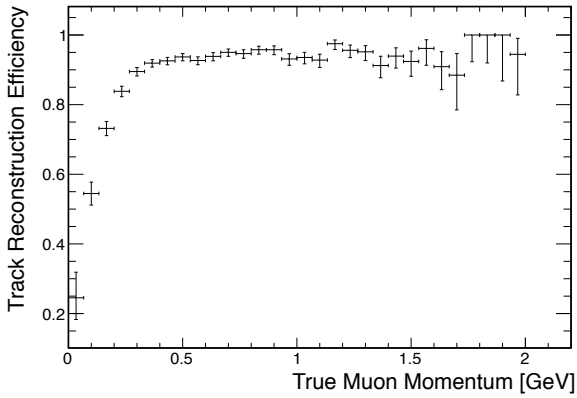

Figure 3: ν_μ CC-induced muon track reconstruction efficiency as a function of the true muon momentum for all ν_μ CC interactions in the fiducial volume. Note that this efficiency slightly differs from the one quoted in [26] as a different cosmic removal pass is being used and a categorization of the 3D reconstructed object as a track is required here.

3.4 Neutrino reconstruction performance

Fig. 3 shows the efficiency of reconstructing muons tracks from ν_μ CC interactions using `PandoraNu` as a function of the muon true momentum after the cosmic removal inside the fiducial volume. A muon from a ν_μ CC interaction is counted as reconstructed successfully if there is a reconstructed track associated to the hits caused by the simulated muon. The overall muon reconstruction efficiency is 90%.

`PandoraNu` reconstructed objects are used in this analysis from here on. `PandoraNu` reconstruction identifies a neutrino interaction vertex and uses it to aid the reconstruction of all particles emerging from the vertex position. There is careful treatment to reconstruct tracks and showers. A parent neutrino particle is created and the reconstructed visible particles are added as daughters of the neutrino.

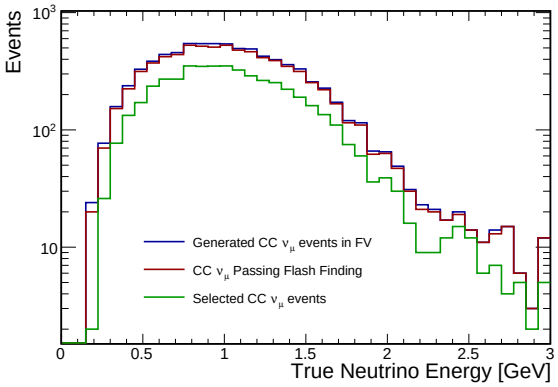

Figure 4: The blue histogram shows the simulated neutrino energy distribution for ν_μ CC in FV, while the red one shows it immediately after the 50 PE cut on the beam spill selected flash. For reference, the green histogram shows the distribution of the final selected signal events.

4 Event Selection

The first step in the event selection is to remove events where no significant optical activity has been detected in coincidence with the neutrino beam spill time. Since typically only one beam spill in 600 will produce a neutrino interaction in the detector, such a requirement will substantially reduce the number of background events. We require that there is at least one flash with more than 50 photoelectrons (PE) integrated over all PMTs in the 1.6 μs beam spill time window. Fig. 4 shows the effect of this cut on the true neutrino energy distribution. The blue curve shows the distribution of the generated events as a function of the true neutrino energy, while the red curve shows the same distribution but only for events that pass the software trigger and this 50 PE cut. The inefficiency due to this cut, which is more stringent than the software trigger cut, is small and negligible for this analysis, and only at the low-energy end of the spectrum.

This analysis makes full use of the MicroBooNE optical detectors to match the flash identified in the 1.6 μs beam window to a single TPC track (or more tracks belonging to the same interaction) that induced that flash. First, a PE hypothesis per PMT (or flash hypothesis) is constructed for every reconstructed interaction in the TPC to understand which one best matches the reconstructed flash. Since the start time t_0 (or correct position along the drift direction x) of each TPC track is not known, the hypothesis is generated for several x positions in the TPC in order to pick the one that matches best. An example of flash-matching is shown in Fig. 5a for MC, and in Fig. 5b for data. This track-to-light matching is crucial to the mitigation of the high cosmic rate, and the successful completion of many MicroBooNE analyses.

The best flash-matched reconstructed interaction is then required to contain at least one reconstructed track. Several algorithms will then check the quality of the fitted track, by looking at the spatial dispersion of the reconstructed hits w.r.t. the

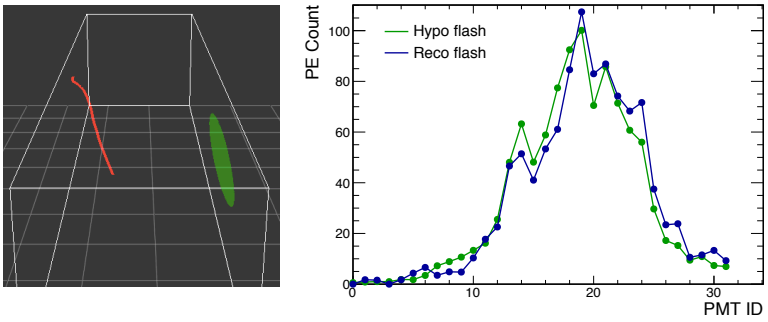

(a)

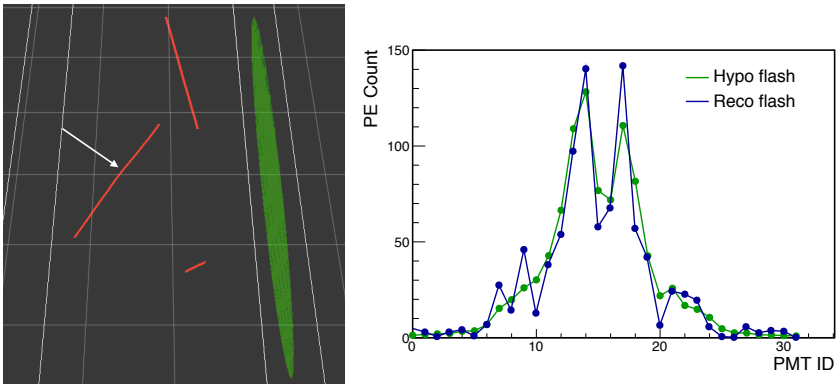

(b)

Figure 5: An example of Flash to TPC Object matching from MC (a) and data (b). The left picture shows a candidate neutrino-induced reconstructed muon track (red) and the reconstructed flash (green) inside the MicroBooNE TPC (white). The right plot shows the flash hypothesis (PE per PMT) in green and the matched reconstructed flash in blue.

track hypothesis.

In order to select CC over NC interactions, a muon candidate track in the interaction needs to be identified. Usually the muon candidate is the longest track in the interaction, but it may happen that the proton is the longest track or that a pion is produced in the interaction, leaving a track longer than the muon. A Support Vector Machine algorithm [28] is used to classify muons and protons given the value of track length and truncated mean dQ/dx.

Fig. 6 shows the distribution of muons (red dots) and protons (blue dots) in the track length - track dQ/dx space. The output of the classifier is shown with light red and blue regions. If a track falls in the blue region, it will be rejected as a muon candidate.

Given a flash-matched 3D reconstructed object in the TPC, the candidate muon track is the longest track of all 3D reconstructed objects in the event not classified

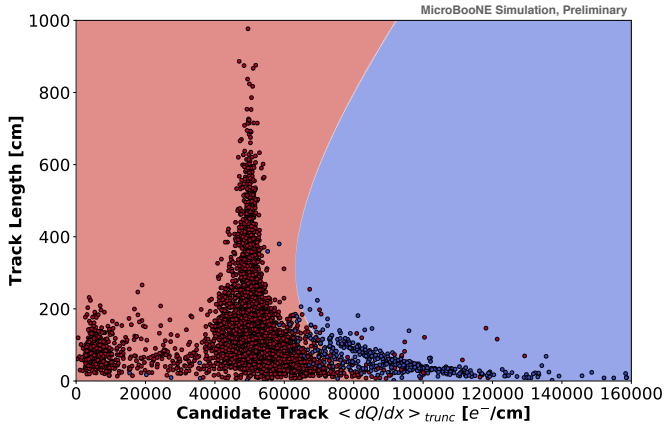

Figure 6: The plot shows the track length as a function of the track dQ/dx for the longest track of all 3D reconstructed objects. Red dots are true muons, blue ones are true protons. The light red and blue regions show the output of the classifier. If a track falls in the blue region, it will not be considered as a muon candidate.

as a proton.

The final goal is to provide a measurement of the cross section as a function of muon momentum. The technique used to estimate the momentum is based on evaluating the MCS of the candidate muon track and is described in more details in Appendix A. The strength of this algorithm is that it can estimate the muon momentum for contained as well as exiting muon tracks. Fig. 7 shows the distribution of the true and reconstructed p_μ as well as for $\cos\theta_\mu$. θ is the angle w.r.t. the beam direction. The angle definitions are shown in Fig. 8 for reference. In the $\cos\theta_\mu$ plot, a negative slope is visible, due to events that are mis-reconstructed in the wrong direction. This slope is embedded in the migration matrix (see following) and, thus, will allow an accurate measurement of the differential cross section, $d\sigma/d\cos\theta$, in terms of the reconstructed $\cos\theta$.

For contained tracks the MCS momentum can be compared with the range-based momentum to understand the quality of the track (see plots in Appendix A). If a track is broken because of mis-reconstruction, the two momentum estimations will not agree. This technique is used to reject split tracks.

4.1 Selected Event Distributions

Fig. 8 shows the final event distributions of the selected candidate track's reconstructed muon momentum and of the cosine of the muon angle. The black data points represent on-beam data with statistical error bars.

Neutrinos don't interact in every event, and some events only contain cosmic rays. The on-beam data sample contains both types of events: events where a neutrino interaction is present, and events where no neutrino interacted in the detector (a purely cosmic event). Off-beam data are taken with the same configuration as on-beam data, but during periods when the neutrino beam was off. Off-beam data events are scaled to match the same beam exposure as the on-beam data. These

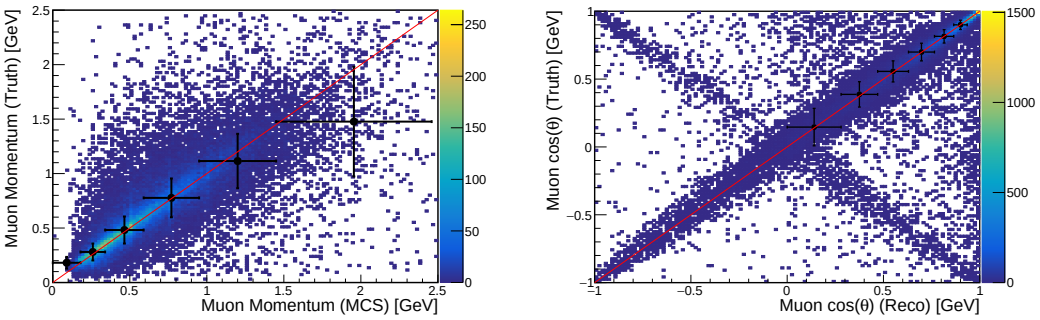

(a) (b)

Figure 7: Distribution of the true vs. reconstructed muon momentum on the left and cosine of the muon angle on the right. The black points on the left plot show the size of the chosen bins (horizontal error bars) for the final single differential cross section measurement. The vertical error bars cover 1σ of the true values in each reconstructed bin. The bins have been chosen such that the horizontal and vertical error bars are the same. The population of tracks with negative slope in stems from tracks with mis-reconstructed direction. This effect is taken into account in the later cross section analysis in the migration matrix constructed from above plots.

events contain only cosmic events and are shown as the shaded blue histogram. For the cross section analysis, a subtraction of off-beam from on-beam data subtracts the background of events of purely cosmic events entirely data-driven. In the remaining events a neutrino interaction is present, but a cosmic in the same event, overlaying the neutrino interaction, may still be falsely selected.

The coloured histograms represent the MC expectation for the signal events and for the MC estimated backgrounds. The MC is normalised to the same POT as the data. The different backgrounds are composed of the following:

(Anti-)Electron Neutrinos These are events where an interaction from a ν_e or

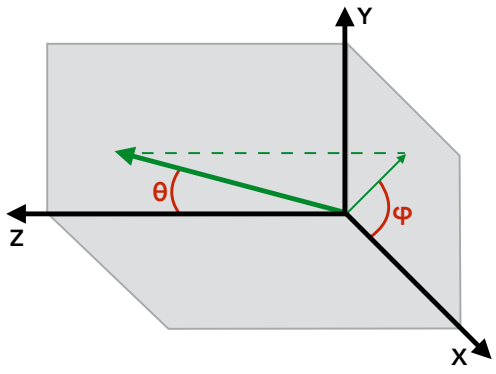

Figure 8: MicroBooNE coordinate system showing the definition of the polar angle θ and the azimuthal angle ϕ for a given track (green). The neutrino beam runs along the z axis, y is the vertical. The TPC electric field runs along the x direction.

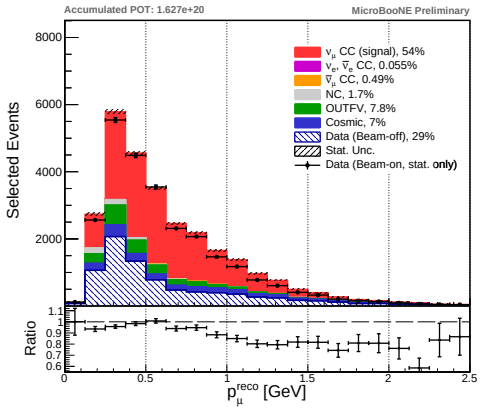

(a) Default GENIE + Emp. MEC.

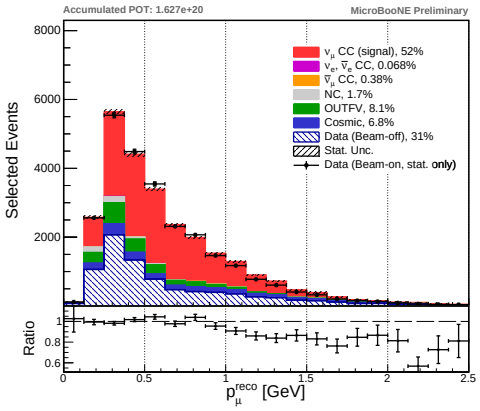

(b) GENIE Alternative.

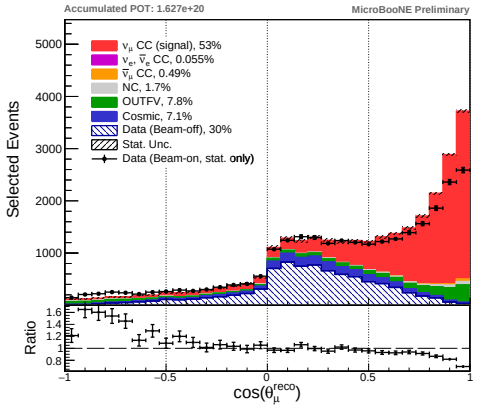

(c) Default GENIE + Emp. MEC.

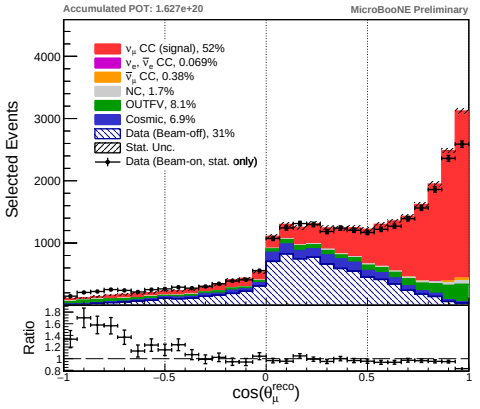

(d) GENIE Alternative.

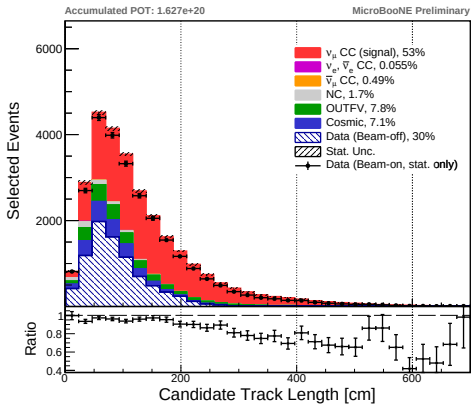

(e) Default GENIE + Emp. MEC.

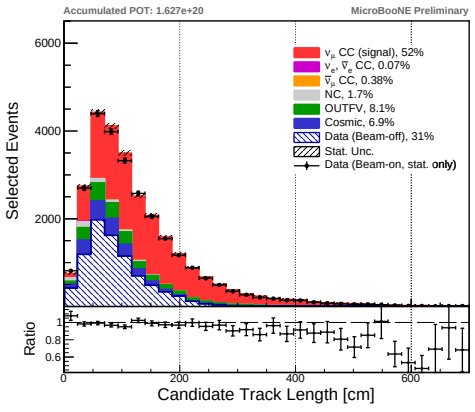

(f) GENIE Alternative.

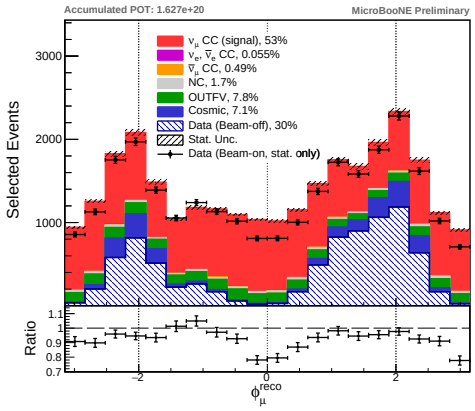

(g) Default GENIE + Emp. MEC.

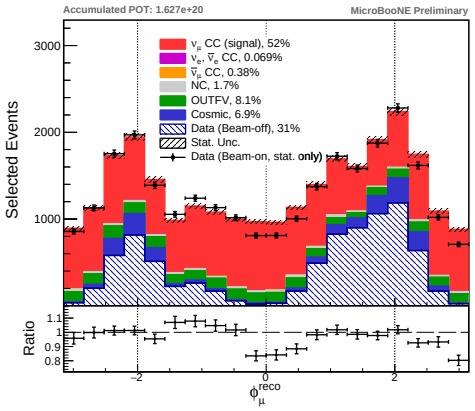

(h) GENIE Alternative.

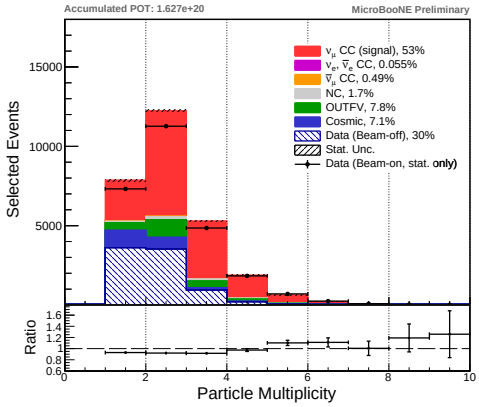

(i) Default GENIE + Emp. MEC.

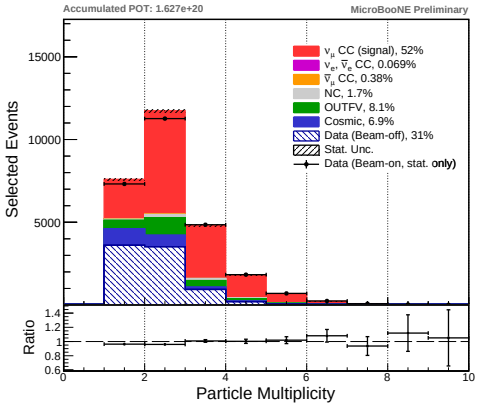

(j) GENIE Alternative.

Figure 8: Final event distributions for the presented selection. The black data points symbolise on-beam data with statistical error bars. The stacked coloured histograms represent the Monte Carlo, with the hashed bands representing the statistical uncertainty only. The red histogram shows signal events. The hashed histogram is off-beam data that has been added to the MC as a data-driven estimate of purely cosmic backgrounds. Data and MC correspond to 1.627×10^{20} POT. The left plots show MC from the default GENIE model set, and the right plots show comparisons to the alternative GENIE model set. The on-beam data points are identical in both plots.

a $\bar{\nu}_e$ interaction is selected. Intrinsic ν_e and $\bar{\nu}_e$ are a tiny contamination in the BNB beam. This usually happens because the electron is identified as a track instead of an electromagnetic shower and is very rare in this analysis.

Anti-Muon Neutrinos These are events where a muon from a $\bar{\nu}_\mu$ interaction is selected. $\bar{\nu}_\mu$ are a small contamination in the BNB beam. Note that MicroBooNE does not have the presence of a magnetic field that can help distinguish a $\bar{\nu}_\mu$ from a ν_μ.

Neutral Current (NC) Those are events where a neutral current event is selected, typically because a pion or a photon induced shower are reconstructed as a track instead of a shower.

Neutrinos interacting outside the Fiducial Volume (OUTFV) These are events where the neutrino interacts outside the fiducial volume, but produces a muon that crosses (or stops in) the TPC, that is then selected. In this case the vertex will definitely be mis-reconstructed and placed at the wrong end of the muon track, leading to wrong momentum and angle reconstruction. These events are not signal events as the true neutrino interaction vertex is outside the FV.

Cosmic These are events where a neutrino interaction is present (usually producing optical activity in the beam window), but a cosmic-ray interaction is selected instead. Some cosmics will enter the TPC from dead regions of the detector, as so may look as contained tracks. This is responsible for some cosmic background.

Table 2 shows the background contamination percentages.

4.1.1 Features in Event Distributions

The event distributions in Fig. 8 show the statistical uncertainty only. Within statistics, we observe a few differences between data and MC in dynamical ($\cos(\theta_\mu)$), overall normalisation) and non-dynamical (ϕ_μ) variables as shown in Fig. 8. These differences appear largely independent of the choice of models in GENIE, but are mitigated in some bins for the alternative set of GENIE models. A complete understanding of the detector model which properly takes into account factors such as space charge [29] and induced charge on the wires is currently under development. For this reason, conservative systematic uncertainties are assigned to these effects. This reduces the significance of the data and MC differences considerably. The following sections describe the observed data/MC discrepancies.

Overall normalisation The comparison of the overall normalisation shows that there is a slight deficit of data events w.r.t. both MC predictions, the default and the alternative. The data/MC ratio is 0.95 for the default, and 0.99 for the alternative. However, this difference is not significant once systematic uncertainties are taken into account (see following sections and final results chapter).

Polar angle distribution The distribution of the polar angle shows two interesting features: While the MC is strongly peaked in the forward/beam direction (in default even more so than in the alternative), the data is less forward peaked. Modeling of neutrino interactions does strongly affect this region of the phase space, however this is also a direction of particular orientation w.r.t. the detector geometry. Therefore, there are also detector systematic effects (for example due to the coherent noise removal) that can have a similar influence on the angular distributions. These effects are currently under investigation. When taking into account systematic uncertainties, the differences become much less significant and a discrimination between the two different model sets can not be made at this point. The other feature is an excess of data events in the backwards region around $\cos(\theta_\mu) \approx -0.7$. These events have been studied and are due to neutrino interactions in the surroundings of the detector hall or rock that enter the detector volume from the upstream end and stop within the first two meters of the TPC. Neutrino interactions outside the cryostat volume are not simulated here, but will be included in a future iteration.

Azimuthal distribution The azimuthal distribution is expected to be unaffected by neutrino interaction model differences but rather subject to detector simulation effects and cosmic simulation. The ϕ distributions of both the default and the alternative show a small deficit of data w.r.t. MC in the regions of $\phi = 0$ and $\phi = \pm\pi/2$. These angles correspond to tracks moving exactly towards or away from the anode wire plane in the x-z plane. The differences between data and MC are attributed to an imprecise modeling of the charge induction [30, 31], which is a topic to be addressed in a future iteration.

Appendix C shows additional distributions of the neutrino reconstructed vertex for data and MC. Shape agreement is important in these distributions as they are not affected by modeling of the interaction process.

Signal and Background	Composition [%]
ν_μ CC in FV (signal)	53.20
Cosmic in BNB	7.06
OUTFV	7.75
NC	1.65
$\bar{\nu}_\mu$	0.49
ν_e and $\bar{\nu}_e$	0.06
Cosmic Only (data)	30.01

Table 2: The table shows the signal and background composition after the event selection.

4.2 Event Selection Performances

The efficiency of the selection is defined in the following way:

$$\epsilon = \frac{\text{Selected } \nu_\mu \text{ CC interactions with true vertex in the FV}}{\text{Generated } \nu_\mu \text{ CC interactions with true vertex in the FV}} \quad (1)$$

while the purity is defined as:

$$p = \frac{\text{Selected } \nu_\mu \text{ CC interactions with true vertex in the FV}}{\text{All selected events}} \quad (2)$$

no cut, of any kind, is applied to the neutrino or lepton kinematics in the efficiency and purity calculation.

The event selection efficiency is shown in Fig. 9a as a function of true muon momentum and in Fig. 9b as a function of true muon $\cos\theta$. The overall selection efficiency is 55.2%, with a purity of 53.2%. The main background is due to cosmics from off-beam data and from events where cosmics are overlaid to neutrino interactions. The second main background is due to neutrino interactions outside the FV.

As nuclear models are dependent on lepton angle and particle multiplicity, this event selection has been carefully designed to minimise biases due to cuts on particle angles or momentum or energy thresholds. Fig. 9d shows the efficiency as a function of the angle around the beam (ϕ). The selection has efficiency across the entire angular phase space.

Fig. 10a shows the efficiency and purity at different stages of the event selection. Fig. 10b shows the efficiency as a function of true neutrino energy for the different GENIE interaction modes: quasi-elastic, resonance, deep-inelastic scattering, meson-exchange current. There is also a negligible contribution from CC coherent pion production events not plotted. All the interaction modes are selected.

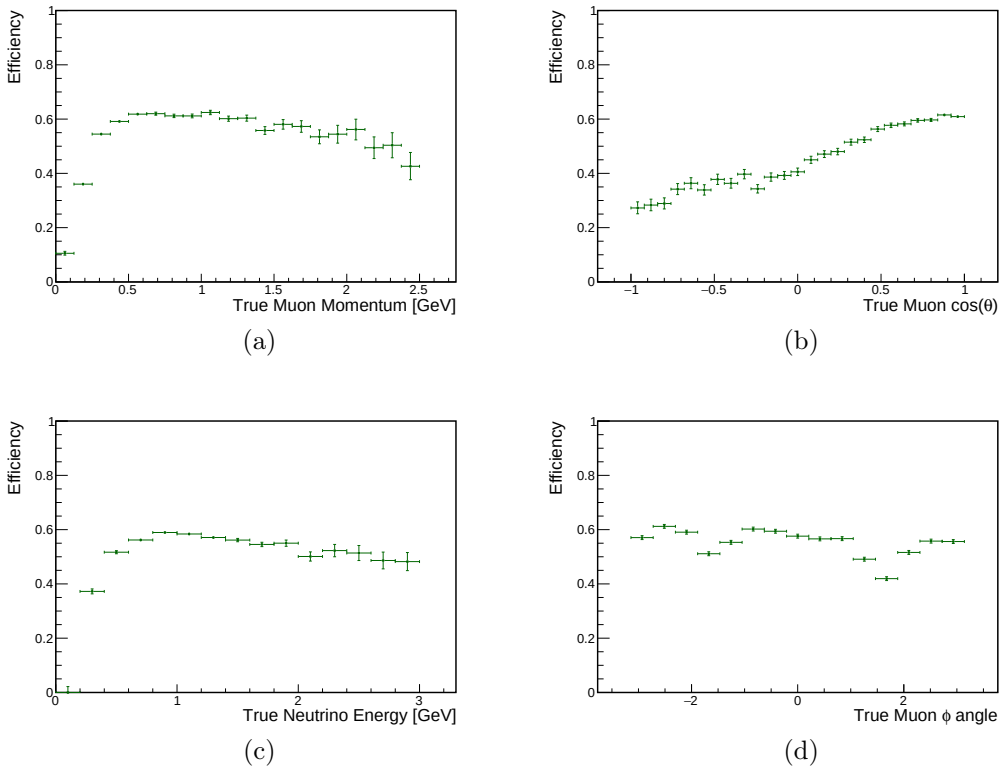

Figure 9: Final selection efficiency (efficiency × acceptance) as a function of the true muon momentum 9a, angle w.r.t. the beam 9b, angle around the beam 9d, true initial neutrino energy 9c. The overall efficiency is 55.2%. The ϕ efficiency distribution is shaped by the cosmic removal.

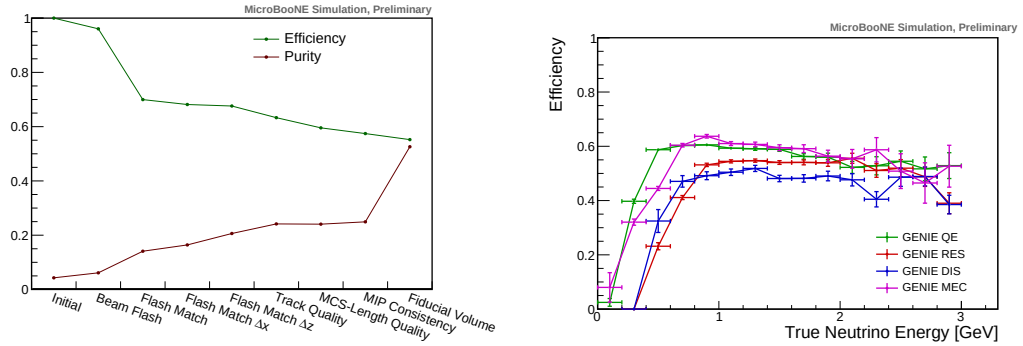

(a) (b)

Figure 10: The left plot shows the efficiency and purity as a function of the event selection cuts. The purity has been calculated by taking into account events from beam-off data as well as events from `BNBCosmic` MC. The right plot shows the efficiency as a function of true neutrino energy for different GENIE interaction modes. There is a negligible contribution from CC coherent pion production events not plotted.

5 Cross Section Measurement

The total flux-integrated cross section is calculated using the following equation:

$$\sigma = \frac{N - B}{\epsilon \cdot N_{target} \cdot \Phi_{\nu_\mu}} \tag{3}$$

where N is the total number of selected data events, B is the number of selected background events (from simulation or off-beam data), ϵ is the efficiency of the event selection (overall, including acceptance), N_{target} is the number of target nucleons and Φ_{ν_μ} is the BNB muon-neutrino flux integrated over all neutrino energies and scaled to the corresponding POT used in this analysis.

In addition to a flux-integrated cross section, the result is also reported as a differential cross section as a function of muon kinematics, i.e. the muon momentum p_μ, which is calculated using the MCS algorithm (see Appendix A), and the cosine of the muon angle θ_μ w.r.t. the beam direction. In this case, signal and background event rates as well as efficiencies are binned as a function of muon momentum or angle:

$$\begin{aligned} \left(\frac{d\sigma}{dp_\mu}\right)_i &= \frac{N_i - B_i}{\tilde{\epsilon}_i \cdot N_{target} \cdot \Phi_{\nu_\mu} \cdot (\Delta p_\mu)_i} \\ \left(\frac{d\sigma}{d\cos\theta_\mu}\right)_i &= \frac{N_i - B_i}{\tilde{\epsilon}_i \cdot N_{target} \cdot \Phi_{\nu_\mu} \cdot (\Delta \cos\theta_\mu)_i} \end{aligned} \tag{4}$$

where N_i and B_i are the selected events binned in reconstructed momentum and $\cos\theta$. $(\Delta p_\mu)_i$ and $(\Delta \cos\theta_\mu)_i$ are the bin widths for bin i in the p_μ and $\cos\theta_\mu$ distributions, respectively. $\tilde{\epsilon}_i$ is the efficiency in bin i, described in the following.

The final result for the single differential cross section measurements is reported as a function of reconstructed kinematic variables, which necessitates using a folded efficiency using the so-called "forward-folding" approach. This requires the conversion of the efficiencies from functions of true kinematics to functions of reconstructed kinematics. This is done using a migration matrix S, which allows to convert the number of true events μ_j in a true bin j, to the number of observed events ν_i in a reconstructed bin i for momentum and angle:

$$\nu_i = \sum_{j=1}^{M} S_{ij}\mu_j \tag{5}$$

where S is given by:

$$S_{ij} = P(\text{observed in bin } i \,|\, \text{true value in bin } j) \tag{6}$$

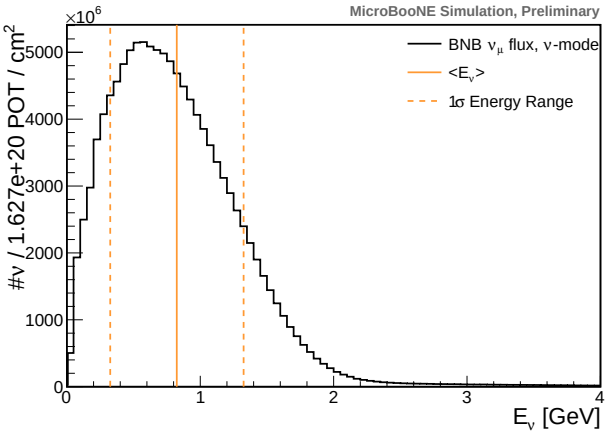

Figure 11: BNB ν_μ CC flux in neutrino mode at the MicroBooNE detector center, scaled to 1.627×10^{20} POT. The lines mark the mean neutrino energy and the 1σ range.

and ν_i and μ_j are the number of events in the reconstructed bin i and true bin j, and M is the total number of bins. The efficiency as function of the reconstructed quantities $\tilde{\epsilon}_i$ is given by

$$\tilde{\epsilon}_i = \frac{\sum_{j=1}^{M} S_{ij} N_j^{\text{sel}}}{\sum_{j=1}^{M} S_{ij} N_j^{\text{gen}}}, \tag{7}$$

where N_j^{sel} is the number of signal selected events in true bin j, and N_j^{gen} is the number of generated signal events in true bin j.

5.1 Input Parameters

The BNB ν_μ flux in neutrino mode running is shown in Fig. 11. The total integrated flux scaled to 1.6×10^{20} POT is

$$\Phi_{\nu_\mu} = 1.16 \times 10^{11}\,\text{cm}^{-2} \tag{8}$$

The mean neutrino energy for the BNB flux is

$$\left\langle E_{\nu_\mu} \right\rangle = 823\,\text{MeV}, \tag{9}$$

with 68% of the values falling into the energy range of $823 - 498 = 325$ MeV and $823 + 502 = 1325$ MeV.

The number of target nucleons in the fiducial volume is calculated as follows:

$$N_{target} = \frac{\rho_{\text{Ar}} \cdot V \cdot N_A \cdot N_{\text{nucleons}}}{m_{\text{mol}}} = 2.64218 \times 10^{31} \tag{10}$$

where ρ_{Ar} is the liquid argon density, V is the fiducial volume, N_A is the Avogadro number, N_{nucleons} is the number of nucleons per argon nucleus, and m_{mol} is the

number of grams per mole of argon. Uncertainties on temperature and pressure are negligible when compared to the flux and detector systematic uncertainties.

The systematic uncertainty on the number of targets is deemed negligible (less than 0.1% coming from the uncertainty on the measured temperature in the cryostat).

6 Systematic Uncertainties

The three main categories of systematic uncertainties affecting this measurement are:

Cross Section: Uncertainties arising from the parametrisation of the models in our neutrino event generator, GENIE.

Beam flux: Uncertainties related to the neutrino flux prediction that is used to calculate the cross section.

Detector effects: Uncertainties related to modeling the detector response. They primarily affect reconstructed quantities, which in turn affect the predicted background event rates and signal efficiencies.

Uncertainties, both statistical and systematic, are encoded in the covariance matrix, E. The total error matrix that will be evaluated is a combination of the statistical and systematic errors:

$$E = E^{\text{stat}} + E^{\text{syst}}, \tag{11}$$

where E^{stat} is the completely uncorrelated statistical error matrix (diagonal), and E^{syst} is the systematic covariance matrix. The total systematic covariance matrix is a combination of independent matrices constructed for each of the categories of systematic uncertainties considered:

$$E^{\text{syst}} = E^{\text{flux}} + E^{\text{xsec}} + E^{\text{detector}}, \tag{12}$$

E_{ij} is the total systematic covariance matrix, with matrix element units of cm^4/GeV or cm^4 for the differential cross section in muon momentum and angle respectively. The evaluation of these three systematic covariance matrices depends on the technique used to evaluate such uncertainties. For the cross section and flux systematics we use a *multisim* technique, which consists of generating several MC replicas, each one called a "universe" where parameters in the models are varied

within their uncertainties, taking into account their correlations. N_s such universes are then created that can be combined to construct the covariance matrix:

$$E_{ij} = \frac{1}{N_s}\sum_{s=0}^{N_s}(\sigma_i^s - \sigma_i^{cv})(\sigma_j^s - \sigma_j^{cv}), \tag{13}$$

where i and j correspond to reconstructed bins (either in muon momentum or muon angle), σ_i^{cv} is the central value cross section in bin i (shown in the previous Chapter), and σ_i^s is the new cross section evaluated in universe s. Note that the beam-on and beam-off data is un-touched in every universe: what changes is the MC only, i.e. efficiency, migration matrix and subtracted background event counts (and integrated flux for flux systematics only).

A different strategy is followed for the detector systematics. In this case *unisim* samples are generated, where only one detector parameter is changed at a time. The change corresponds to one standard deviation. The difference between the central value cross section and the cross section calculated with the new MC simulations with modified parameters gives an indication of the systematic uncertainty on the cross section. The covariance matrix can be constructed in the following way:

$$E_{ij}^{det} = \sum_{m=1}^{u}(\sigma_i^{cv} - \sigma_i^m)(\sigma_j^{cv} - \sigma_j^m), \tag{14}$$

where σ^m is the cross section extracted using MC systematic run m. u is the number of *unisims*.

The fractional covariance matrix is generally a more useful result and is defined as

$$F_{ij} = \frac{E_{ij}}{\sigma_i^{cv}\sigma_j^{cv}}. \tag{15}$$

6.1 Cross Section Uncertainties

GENIE provides a built-in framework of event re-weighting for evaluating systematic uncertainties in an analysis [14, 24]. Given a certain physics parameter P with estimated prior uncertainty δP, the parameter can be re-weighted to $P' = P + x_p\delta P$. x_P is a systematic parameter. For this analysis, the standard GENIE re-weighting parameters are used [24].

Fig. 12a shows exemplary how the number of events changes if one parameter is increased or decreased by $\pm 1\sigma$ as a function of the outgoing muon momentum using the axial mass for CC quasi elastic interactions. The efficiency does not change much, since it is a ratio of two re-weighted distributions. The effect on the

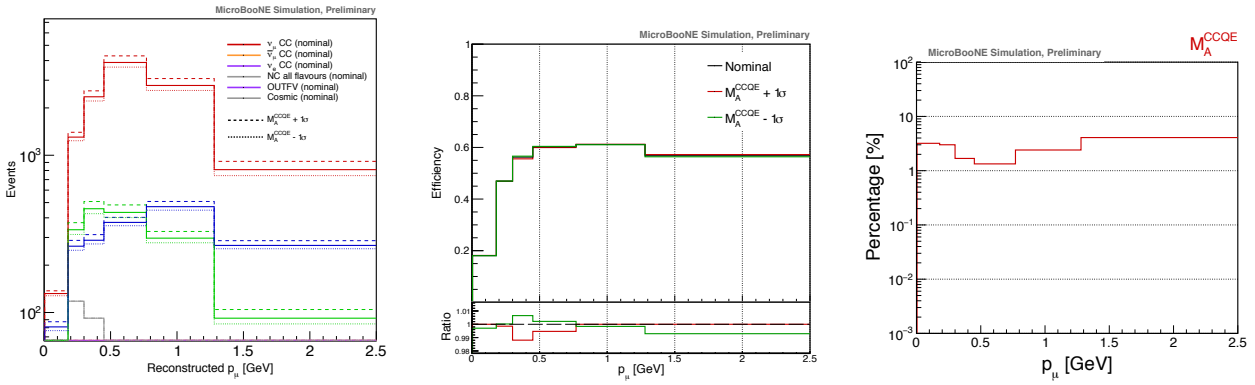

(a) Number of events (b) Selection efficiency (c) Cross section percental difference

Figure 12: The three plots show the effect of changing M_A^{QE} by $\pm 1\sigma$ on the reconstructed momentum distribution of the final selection. 12a shows the number of events and is decomposed in signal (red) and GENIE related backgrounds (green, violet, orange and grey). The blue line shows cosmic events that happen together with a neutrino interaction. Those are usually selected as they contain a neutrino induced flash and therefore these events are also re-weighted. Cosmics from off-beam data are not re-weighted. The solid line shows the distribution for the nominal value of the GENIE parameters, the dashed line if the parameter is increased by 1σ and the dotted line if decreased by 1σ. 12b shows the efficiency for nominal values and variations of $\pm 1\sigma$. 12c shows an estimate of the impact on the total extracted cross section from changing M_A^{QE} by $\pm 1\sigma$.

final cross-section is also estimated based on the relative difference

$$\left| \frac{\sigma - \sigma^{\pm}}{\sigma} \right|, \tag{16}$$

where σ is the cross section measured with the central value MC, and $\sigma^{\pm}$ is the cross section measured by re-weighting the cross section while tweaking the desired parameter by $\pm 1\sigma$.

For the actual analysis, the systematic uncertainties arising from cross section modeling are evaluated by re-weighting all GENIE parameters simultaneously. For the evaluation, 100 multisim universes are generated using the re-weighting machinery and cross sections for each universe are extracted in order to estimate the total uncertainty (see Fig. 13). The total cross section relative uncertainty from cross section modeling evaluated using GENIE amounts to 4%.

Fig. 14 shows the same result as a function of muon kinematics. The top plots show the cross section distributions among the 100 universes. The universes produce variations of the result distributed around the nominal value.

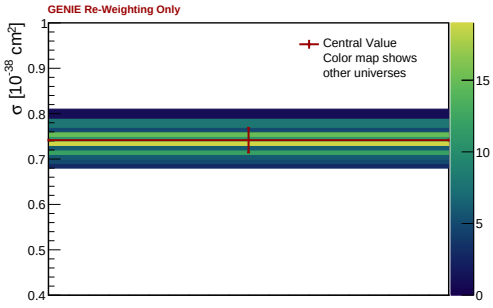

Figure 13: Total cross sections extracted from data for all simulated GENIE universes represented by the colour map. The red graph shows the result for the nominal MC. The red error bars indicate the GENIE systematic uncertainty only, derived from the multisims according to equation 13. The relative systematic uncertainty on the total cross section is 4%.

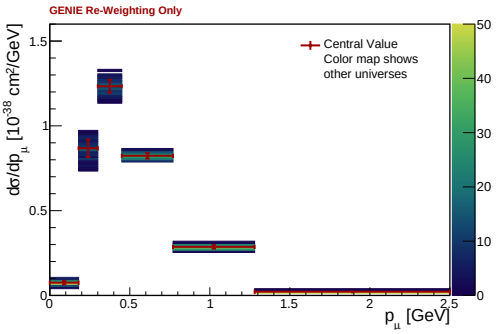

(a) Data extracted cross sections.

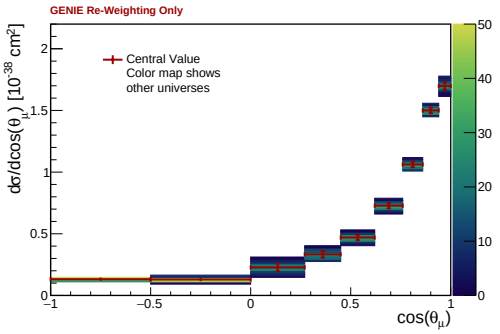

(b) Data extracted cross sections.

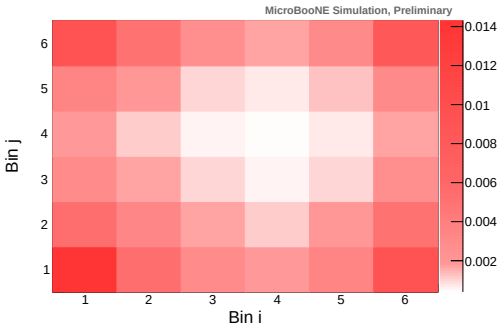

(c) Fractional covariance matrix for p_μ.

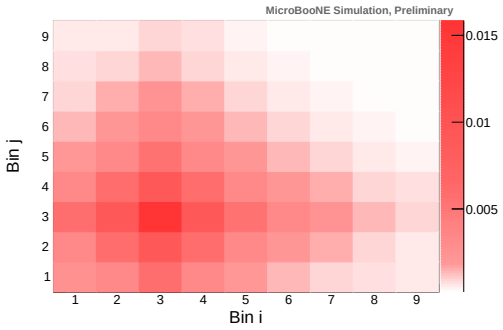

(d) Fractional covariance matrix for $\cos\theta_\mu$.

Figure 14: Plots 14a and 14b show the total cross section extracted from data as a function of muon momentum and angle for all the simulated universes in the colour map. The red graph indicates the nominal MC result. The red error bars indicate the GENIE systematic uncertainties only, derived from the *multisims* according to equation 13. Figures 14c and 14d show the fractional covariance matrices.

Parameter	Description	Total Cross Section Relative Uncertainty
Non-Hadron	Non-Hadron	5.34%
K^- Production	K^- production cross section	0.50%
K^+ Production	K^+ production cross section	0.55%
K^0 Production	K^0 production cross section	0.51%
π^- Production	π^- production cross section	0.73%
π^+ Production	π^+ production cross section	9.69%
Total	Combined uncertainty	11.93%

Table 3: Flux systematics parameters and their contribution to the cross section relative uncertainty.

6.2 Beam Flux Uncertainties

To assess the uncertainties on the neutrino flux prediction, the final flux simulation from the MiniBooNE collaboration is utilised after being ported into the `LArSoft` framework [12]. The uncertainties due to beam flux modeling are divided into two main categories:

- uncertainties related to hadron production (π^+, π^-, K^0, K^+, K^-) that arise due to uncertainties in the production of secondary particles when protons collide with the beryllium target.
- all other related uncertainties, which are here called "non-hadron". These uncertainties arise from errors in estimating the current that runs in the horn conductor, the depth by which such current penetrates the conductor ("skin effect"), and the pion and nucleon cross sections (total, inelastic, and quasi-elastic) on aluminium and beryllium.

1000 multisims with varied flux parameters were generated. For the non-hadron uncertainties, they are estimated first by varying the effect by plus or minus one standard deviation or, in the case of the skin effect, switching the model, which creates a second universe. Then, these two or three universes are used to generate weights to assess the overall systematic uncertainties by assuming they follow a Gaussian distribution around the central value. 1000 weights were generated in this way and the covariance matrix was calculated following Eq. 13.

Table 3 summarizes the individual contributions of flux uncertainties to the total extracted cross section. Figures 15 and 16 illustrate the variations of the extracted cross section result due to flux uncertainties. The total cross section relative uncertainty for the flux systematics amounts to 12%.

The fractional covariance matrices for the muon momentum and $\cos\theta$ distributions have all been calculated according to Eq. 15. As can be seen in Figures 15 and

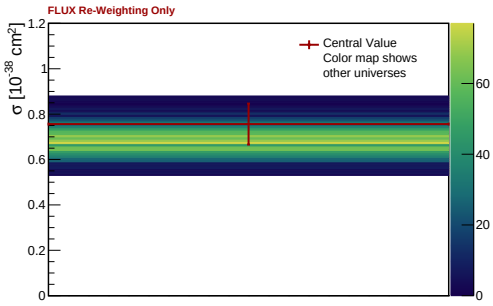

Figure 15: Total cross section extracted from data for all the simulated flux universes represented by the colour map. The red graph shows the result for the nominal MC. The red error bars indicate the flux systematic uncertainty derived from the *multisims* according to equation 13. The relative systematic uncertainty on the total cross section is 12%.

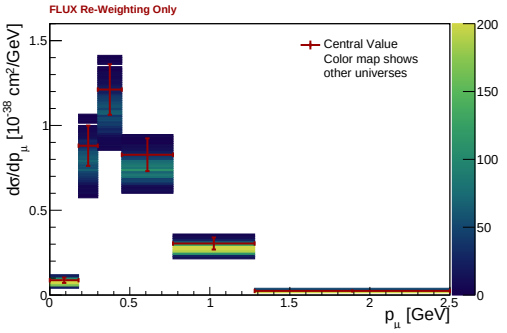

(a) Data extracted cross sections.

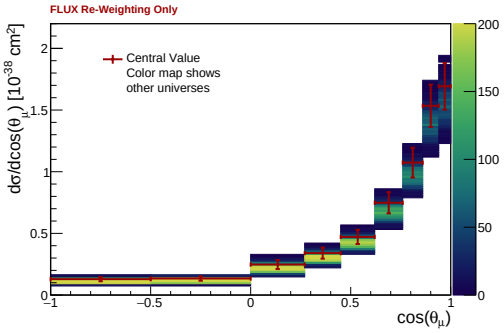

(b) Data extracted cross sections.

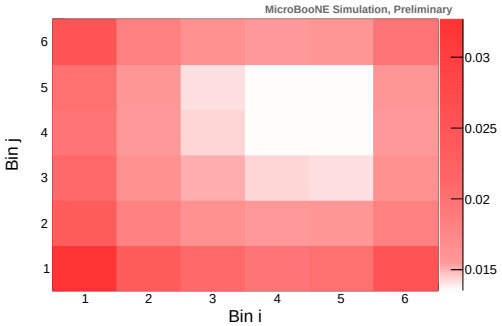

(c) Fractional covariance matrix for p_μ.

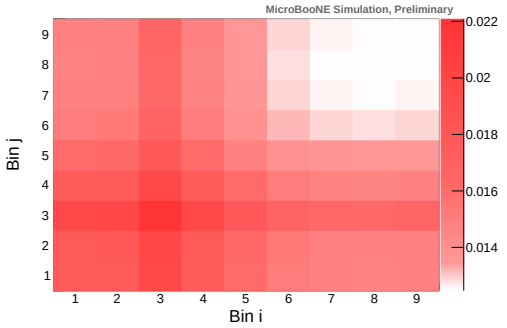

(d) Fractional covariance matrix for $\cos\theta_\mu$.

Figure 16: Plot 16a and 16b show the total cross section extracted from data as a function of muon momentum and angle for all the simulated universes in the colour map. The red graph indicates the nominal MC result. The red error bars indicate the beam flux systematic uncertainties only, derived from the *multisims* according to Eq. 13. Figures 16c and 16d show the fractional covariance matrices.

??, there is a bias of the variation samples and the nominal flux modeling is not identical to the average of the result of all universes. This comes from an inconsistent derivation of systematic uncertainties on the underlying pion production cross

sections when modeling the flux. This bias is taken into account when calculating the covariance matrix by using the nominal result as central value in Eq. 15 and not the average, which makes the total estimated uncertainty conservative.

6.3 Detector Uncertainties

In this section, we describe the detector-related systematic uncertainties. While our understanding of the LArTPC detectors have been improved significantly in the past couple years, there are still areas where further refinements in the simulation are required. At this point, we make conservative estimates of the possible systematic biases in our Monte Carlo and treat them as symmetric 1σ uncertainties.

The detector systematic uncertainties are evaluated via *unisims* and Eq. 14 is used to calculate the covariance matrix. Variation samples for a set of 13 detector parameters have been generated. Variations of the central value were created by using a $\pm 1\sigma$ range for parameters where constraints from data were available, or otherwise by simulating an alternative model. The list of parameters is given in Table 4.

Work is currently ongoing to improve the knowledge on proper uncertainty ranges and detector systematics uncertainties are expected to be improved in the next iteration of this analysis.

The uncertainty on the total cross section related to the above listed detector effects has been calculated and the covariance matrices are shown in Fig. 17. The relative detector systematic uncertainty on the total cross section currently amounts to 19%. Contributions of individual effects are listed in Table 4. For parameters with both plus and minus 1σ variations, we chose the larger of the relative deviations from the central value cross section as an uncertainty in to use in the total error budget. The largest contributing effect is the simulation of induced charge on neighbouring wires. This is an effect that is currently being implemented into the standard simulation and will in the future be a default simulation with a reasonable parameter range for variation, which we expect will significantly reduce the impact of the effect on the measurement.

6.4 Additional Uncertainties

An additional uncertainty is due to POT counting. The primary proton beam is monitored using two toroids measuring its intensity (protons-per-pulse). The proton flux measured in the two toroids agrees to within 2% [12]. This is included as an additional uncertainty on the flux, added in quadrature to the covariance matrices.

Detector Systematic Sample	Description	Type	Total Cross Section Relative Uncertainty [%]
Space Charge	A simple data-driven calibration is applied to the space charge simulation to make it better match measured space charge effects [29].	Modified Model	2.7
Induced Charge	Charge induction is simulated on a longer spatial range than in the default MC, so that more distant wires see the effect of drifting charge.	Alternate Model	15
Light Yield	An improved light production simulation model is used.	Alternate Model	3.7
Remove Channels Prone to Saturating	Turning off channels that frequently become saturated as charge builds up on capacitors in the ASIC circuits, resulting in deadtime.	Alternate Model	2.1
Remove Misconfigured Channels	Turning off the misconfigured channels associated with ASICs that have a different gain and shaping time than desired	Modified Model	2.1
Wire Response Function	The wire response functions used during deconvolution are stretched by 20% based on MicroBooNE data.	$\pm1\sigma$	1.4
Longitudinal Diffusion	The amplitude of longitudinal diffusion is varied based on world data [32, 33].	$\pm1\sigma$	1.4
Transverse Diffusion	The amplitude of transverse diffusion is varied based on world data [34, 35, 36].	$\pm1\sigma$	2.1
Wire Noise	The amplitude of the wire noise model varied.	$\pm1\sigma$	6.4
PE Noise	The single-PE noise of the PMTs is varied.	$\pm1\sigma$	2.1
TPC Visibility	The light yield in the cryostat but outside the TPC is increased by 50%.	Alternate Model	4.3
Lifetime	The electron lifetime is reduced to 10 ms. (This condition affects only about $\sim$10% of data taken with lower purity).	Alternate Model	1.2
Recombination	The Birks recombination model, with parameters derived from ICARUS, is used instead of the default modified box model, with parameters derived from Argoneut.	Alternate Model	1.3
Total combined relative uncertainty			18.7

Table 4: List of parameters varied for the detector systematic studies.

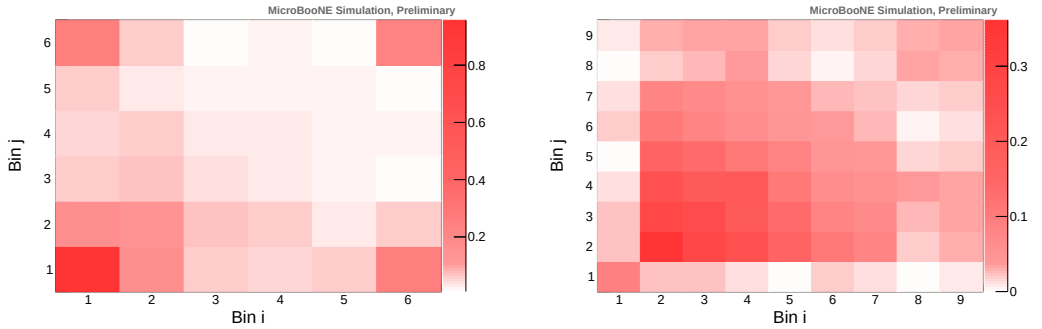

(a) Fractional covariance matrix for p_μ. (b) Fractional covariance matrix for $\cos\theta_\mu$.

Figure 17: The plots show the detector systematic fractional covariance matrices for the muon momentum cross section (left) and the angular cross section (right).

The time of the detected flashes in data is known to have fluctuations of 100 ns. An additional 4% uncertainty takes into account flashes that may be lost because of this fluctuation.

Finally, an uncertainty of 7% to the total cross section is due to uncertainties in our simulated cosmic background. This has been estimated by comparing simulations with the Corsika cosmic model to simulation with a data-driven cosmic model (utilising off-beam data).

Error Source	Method	Estimated Relative Uncertainty
Beam Flux	Estimated with multisim variations	12%
Cross Section Modeling	Estimated with multisim variations	4%
Detector Response	Estimated with unisim variations	19%
POT Counting	Toroids Resolution	2%
Cosmics (in-time)	Estimated from data-driven cosmic model	7%
Cosmics (out-of-time)	Estimated from off-beam statistics	1%
Beam Timing Jitter	Estimated from on- minus off-beam flashes	4%

Table 5: The table shows the different contributions to the total cross section systematic uncertainty.

7 Results

7.1 Flux Integrated Cross Section

The flux integrated cross section is calculated according to Eq. 3. A total of $N = 26339 \pm 162$ data events is selected, with an estimated number of background events $B = 13062 \pm 99$ (errors statistical). For the total cross section, the cross section modeling, flux and detector systematics are added in quadrature to obtain the final flux integrated cross section result:

$$\begin{aligned}\sigma &= 0.756 \pm 0.011\,(\text{stat}) \pm 0.027\,(\text{genie}) \pm 0.114\,(\text{flux}) \pm 0.141\,(\text{det}) \times 10^{-38}\,\text{cm}^2 \\ &= 0.756 \pm 0.011\,(\text{stat}) \pm 0.185\,(\text{syst}) \times 10^{-38}\,\text{cm}^2 \\ &= 0.76 \pm 0.19 \times 10^{-38}\,\text{cm}^2\end{aligned} \tag{17}$$

A summary of all the systematic uncertainties taken into account is shown in Table 5. This measured cross section can be compared to a MC expected cross section for the same flux of

$$\sigma_{\text{MC}} = 0.867 \pm 0.004\,(\text{stat.}) \times 10^{-38}\,\text{cm}^2 \tag{18}$$

This result is compared to the world data plot in Fig. 18. The orange curve shows the GENIE initial cross section spline as a function of neutrino energy. Note that the cross section is divided by the mean neutrino beam energy in this plot. The error bars on the x axis come from the width of out neutrino energy spectrum, see Eq. 9.

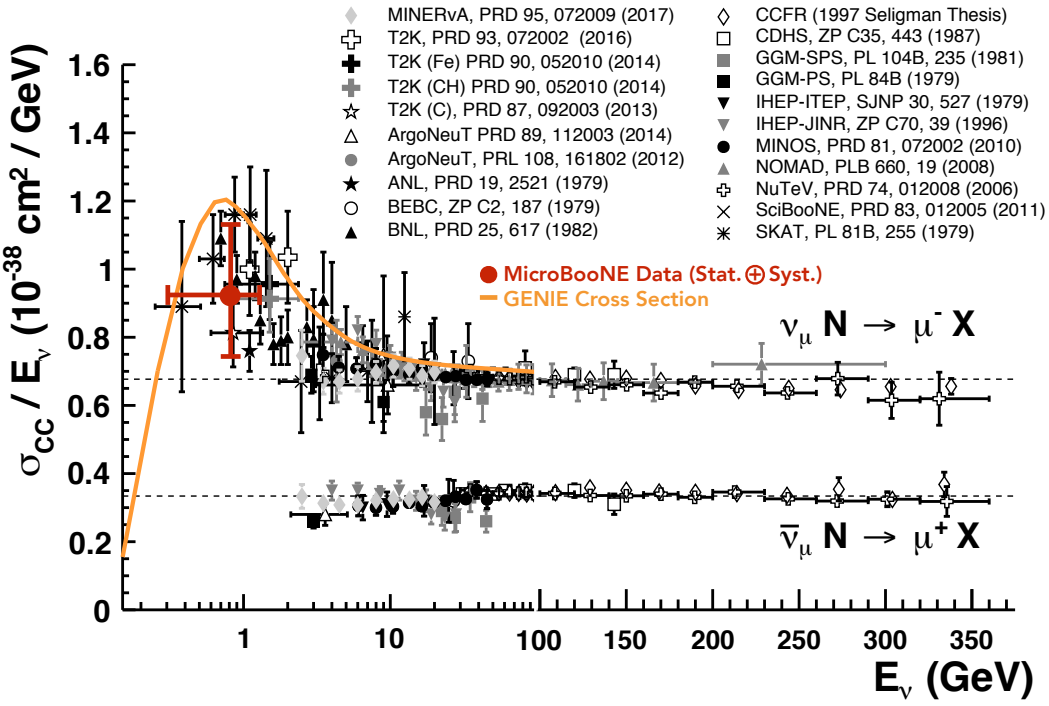

Figure 18: CC inclusive measurements for ν_μ and $\bar{\nu}_\mu$ from different experiments with different nuclear targets in black and grey. The red point represents the result from this analysis. The error bars show the sum in quadrature of the statistical and systematic uncertainties. The error bars on the x axis come from the width of out neutrino energy spectrum, see Eq. 9. The orange curve shows the GENIE cross section spline as a function of neutrino energy.

7.2 Single Differential Cross Section

The single differential cross section in muon momentum p_μ and cosine of the muon angle $\cos\theta_\mu$ were calculated according to Eq. 4. The ν_μ CC inclusive single differential cross section results on argon are shown in Fig. 19. The black data points show the data extracted cross section with the inner error bars representing the statistical uncertainty only, while the outer error bars show the sum in quadrature of the statistical and systematic uncertainties. Systematic uncertainties from flux, cross section modeling and detector have been taken into account.

The green and blue distributions show the MC predicted cross section from GENIE for the default model set, and the alternative model set, respectively. The light green and blue error bands represent the statistical uncertainty on the MC.

The total systematic error fractional covariance matrices and correlation matrices are shown in Fig. 20 for both p_μ bins, and the $\cos\theta_\mu$ bins.

The results are strongly dominated by systematic uncertainties. The dominant source of systematic uncertainties are detector effects followed by beam flux uncertainties. As mentioned in Section 6.3, this first round of systematic uncertainties has been assessing uncertainties in a very conservative way and a future improved treatment of detector effects will likely decrease the systematic uncertainties on the measurement. Within the currently large uncertainties, the measured cross section largely agrees with the predicted cross section by both GENIE model sets shown here. A deviation between the measured cross section and the prediction is observed in the very forward going phase space, corresponding to values of $\cos(\theta_\mu) \leq 1$. It can be seen the model set labeled GENIE alternative is less peaked in the forward direction and is closer to the measurement. However, a definitive statement requires a stronger constraint of systematic uncertainties in the measurement.

8 Future Improvements

Several improvements are currently being carried out to improve this analysis. The systematic uncertainties are still preliminary and conservative. There is a current effort to better understand and improve the detector systematics, and to refine the central value MC. Additional studies of dirt interactions (neutrinos that interact outside the cryostat) are underway, though their expected contribution is small. This analysis will also move to a double differential cross section measurement in the very near future.

We also expect improvements in our event reconstruction and selection. A Cosmic Ray Tagger (CRT) has recently been installed and can be used as a muon telescope to help identify and further reject cosmic rays. Updated electronics boards that introduce less noise into the detector have been installed, which will improve

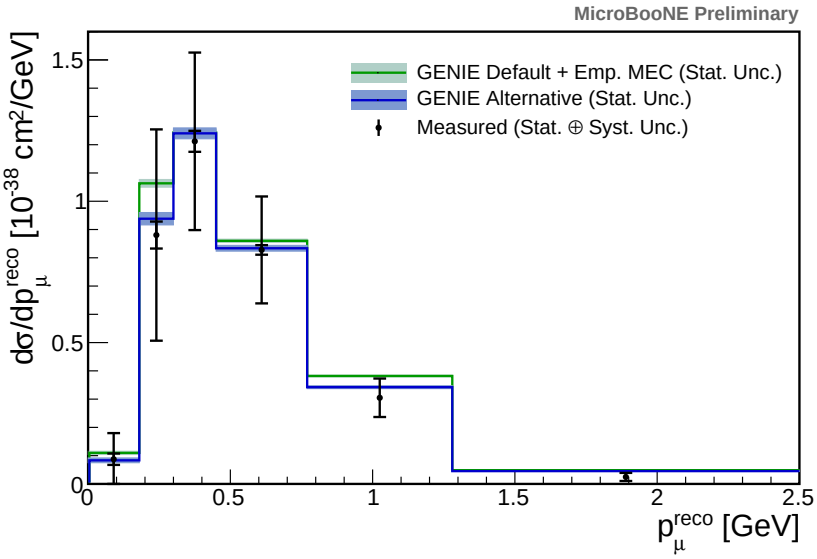

(a)

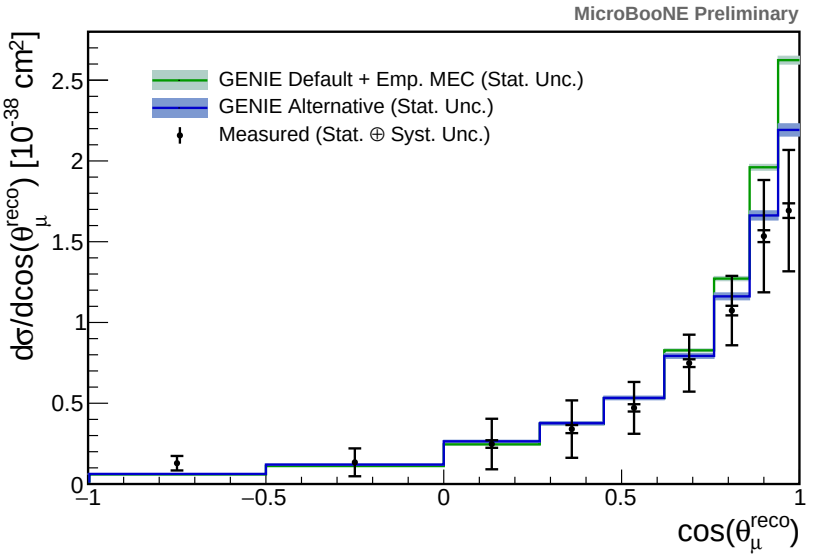

(b)

Figure 19: ν_μ CC inclusive differential cross section on argon as a function of the reconstructed muon momentum and cosine of the muon polar angle. The black data points show the data extracted cross section (using default GENIE for background and efficiency estimation), while the green and blue curves shows the MC predicted cross section from GENIE default and alternative model sets respectively. The data cross sections contain flux, cross section modeling and detector systematic uncertainties.

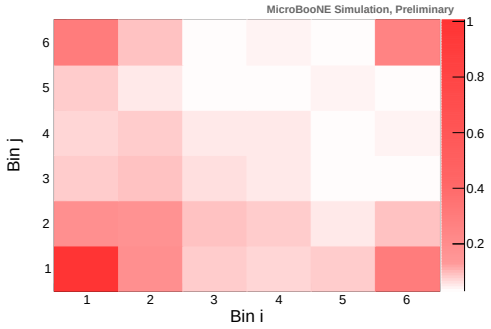

(a) Fractional systematic covariance matrix for the p_μ bins.

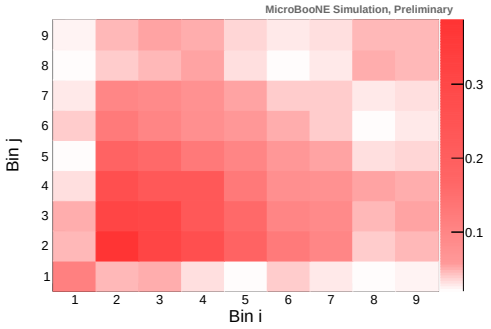

(b) Fractional systematic covariance matrix for the $\cos\theta$ bins.

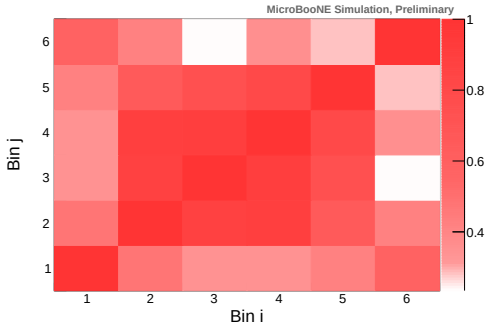

(c) Systematic correlation matrix for the p_μ bins.

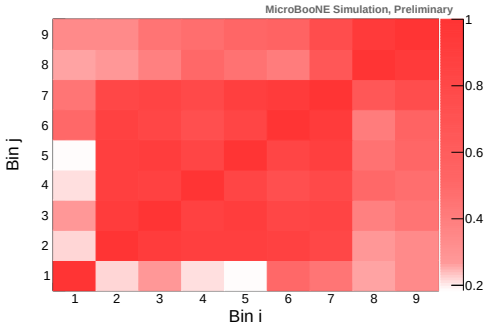

(d) Systematic correlation matrix for the $\cos\theta$ bins.

Figure 20: The total systematic error fractional covariance matrices (upper plots) and correlation matrices (bottom plots) for both the p_μ bins and for the $\cos\theta$ bins.

our noise filtering. Finally, this current event selection is being used to validate improvements in the event reconstruction and particle identification.

9 Summary and Outlook

This note describes the first ν_μ charged-current inclusive cross section measurement with MicroBooNE's Run 1 data (1.6×10^{20} POT). The measurement has been presented with flux, cross section modeling, and detector systematic uncertainties. Of the three groups of systematic uncertainties, the detector systematics are currently the dominant uncertainties.

The only published double-differential data from experiments are event distributions from SciBooNE [5] and cross section measurements from the T2K on-axis detector [37], both as a function of muon angle and muon momentum. T2K – which has a comparable beam energy to MicroBooNE – was able to bin in four angular and five momentum bins. In this analysis we were able to bin in nine angular and six momentum bins.

This analysis has full angular coverage and for the first time uses multiple Coulomb scattering to estimate the muon momentum. This allows not to restrict the analysis to only contained tracks (which implies introducing a momentum cut-off), but to include both contained and exiting tracks.

This measurement has been compared with two sets of models available within GENIE, the first one being the default GENIE configuration. In the total cross section, we find agreement with both model sets. In the differential cross section, the data is somewhat closer to the second model set. The difference between models, and also between data and both sets of simulation is largest in the forward region, which comes from the very different quasi-elastic models adopted in the two sets. However, at this point the systematic uncertainties are very large and none of the two model sets can be ruled out. With future improvements to the detector systematics we expect that this inclusive analysis can be sensitive to these model variations. The over-fluctuation in the most backward bin is due to non-simulated background which will be included in the next iteration of this analysis.

Improvements to the analysis are expected in future iterations, together with a more precise understanding of the detector systematic uncertainties, which will improve the precision of this measurement.

A Momentum Estimation

The final goal of this analysis is to provide a measurement of the cross section as a function of muon momentum, which is a direct observable of the experiment and

a kinematic property sensitive to model differences. To estimate the momentum, three different techniques can be used in MicroBooNE:

Momentum by Track Length Assuming the track is a muon track, the momentum p can be estimated since the range of a muon in argon is known given an initial momentum p. This requires the track to be fully contained in the TPC.

Momentum by Multiple Coulomb Scattering (MCS) Assuming the track is a muon track, the momentum can be estimated by looking at how much the muon scatters in argon and comparing it to the theory, which provides the scattering angle as a function of p [27]. This method is powerful as it can also be applied to exiting muons.

Momentum by Calorimetry Information The dE/dx along the track can be measured, and integrated in x to get the energy of the particle, and from there the momentum. This requires the track to be fully contained in the TPC.

While the first and last methods can only be applied to tracks that are fully contained in the detector, the second one can be applied to all tracks. Since a large fraction of muons will exit the detector at the BNB energies, it is important to not restrict the analysis to only contained muons in order to keep the selection efficiency high. Momentum by MCS will therefore be used int his analysis. The MCS momentum is the result of a maximum likelihood method where the likelihood is taken to be the product over all track trajectory segments of the probability of observing that scattering given the prediction [27]:

$$L(\sigma_{0,1},\ldots,\sigma_{0,n};\Delta\theta_1,\ldots,\Delta\theta_n) = \prod_i f(\sigma_{0,i},\Delta\theta_i) \tag{19}$$

where the normal probability distribution with uncertainty σ_0 and mean zero is assumed:

$$f(\sigma_0,\Delta\theta) = (2\pi\sigma_0^2)^{-1/2}\exp\left[-\frac{1}{2}\left(\frac{\Delta\theta}{\sigma_0}\right)\right] \tag{20}$$

and

$$\sigma_0 = \sqrt{(\sigma_0)^2 + (\sigma_0^{\text{res}})^2} \qquad \sigma_0 = \frac{S_2}{p\beta c} z\sqrt{\frac{l}{X_0}}\left[1+\epsilon\times\ln\left(\frac{l}{X_0}\right)\right] \tag{21}$$

σ_0 is given by the Highland formula, β is the ratio of the particle's velocity to the speed of light (assuming the particle is a muon), l is the distance traveled inside the material, z is the magnitude of the charge of the particle (unity, for the case of muons), and X_0 is the radiation length of the target material (taken to

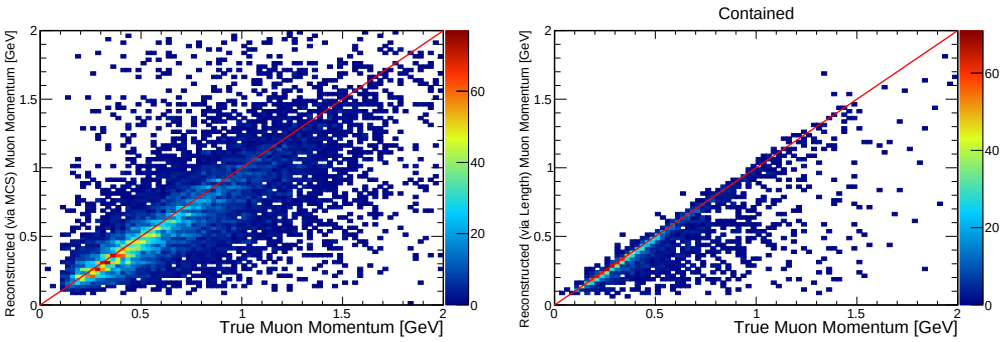

Figure 21: Reconstructed momentum of the muon candidate tracks v.s. truth momentum for muons that are truly originating from neutrino interactions. The left plot shows the momentum estimated via MCS (for all tracks), the right plot shows the momentum estimated via track length (only for contained tracks).

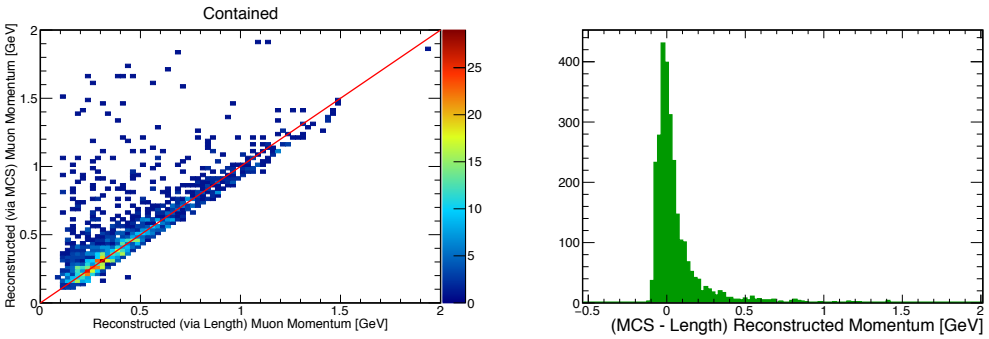

(a) (b)

Figure 22: 22a shows the two-dimensional histogram of the reconstructed muon momentum obtained with the MCS fit (y axis) and with the range-based algorithm (x axis). 22b shows the difference between the two.

be a constant 14 cm in liquid argon). S_2 and ϵ are parameters determined to be 13.6 MeV and 0.038, respectively. MicroBooNE developed a maximum likelihood fit based on a tuned Highland formula for argon where S_2 is replaced with a momentum-dependent parameter $\kappa(p) = (0.105\,\text{MeV})/(p(\text{GeV}))^2 + 11.04\,\text{MeV}$.

The likelihood in Eq. 19 depends on the muon momentum and the maximum likelihood corresponds to the muon momentum estimation.

Fig. 21 shows the reconstructed momentum as a function of the true momentum for two momentum reconstruction algorithms: MCS and track length.

For contained tracks, the comparison between the reconstructed momentum using two different methods can give an indication of the correctness and quality of the track reconstruction. This is shown in Fig. 22. This technique is applied in

this analysis to reject mis-reconstructed muon candidate tracks.

B Monte Carlo Truth Distributions

The plots in Fig. 23 show the distribution of true GENIE simulated variables: neutrino energy, muon momentum, cosine of the muon polar angle, muon azimuthal angle. These distribution are further divided in different GENIE interaction modes. The coloured histograms are stacked. The left plots show the distributions originally generated by GENIE (default model set), while the right plots show the distribution of the selected events only. Apart for a normalisation difference (the efficiency is $\sim 55\%$), one can see that the distributions are not particularly shaped after the selection, so that the event selection is not introducing any particular bias.

C Additional Distributions of the Final Selection

Fig. 24 shows the distribution of the candidate neutrino interaction vertex in the detector for both data and MC. This distributions are interesting since they mostly depend on the modeling of the detector and only to a minor extend on the modeling of the underlying neutrino interaction physics.

The x distribution is shaped because of the space-charge effect [29] and because the flash matching algorithm is more inclined to fail if tracks are close to the anode plane (at $x = 0$). The y distribution shows that there are more cosmics in the upper part of the detector. Those are stopping cosmic muons. The gap in the z distribution is introduced by the fiducial volume definition, and is meant to remove an unresponsive region of the collection plane.

Overall it can be noted that data and MC agree reasonably well, giving some level of confidence in the event simulation chain.

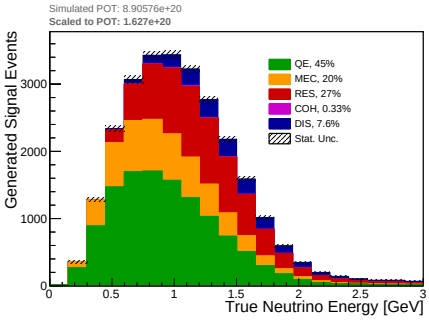

(a) Generated.

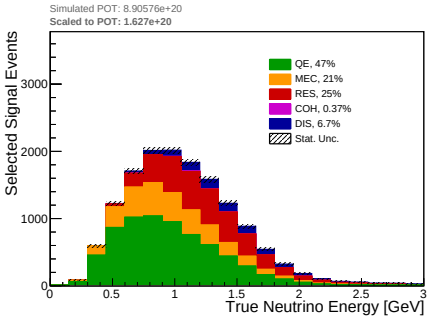

(b) Selected.

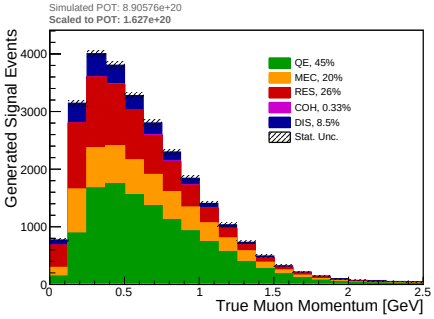

(c) Generated.

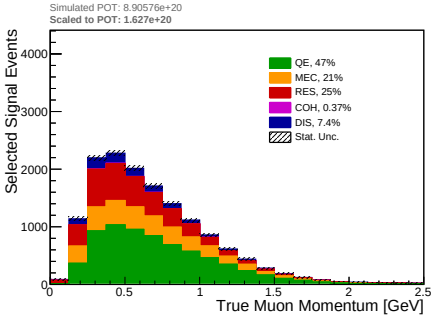

(d) Selected.

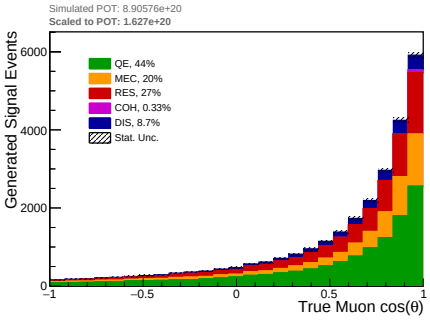

(e) Generated.

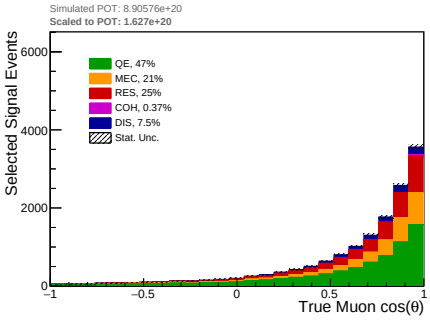

(f) Selected.

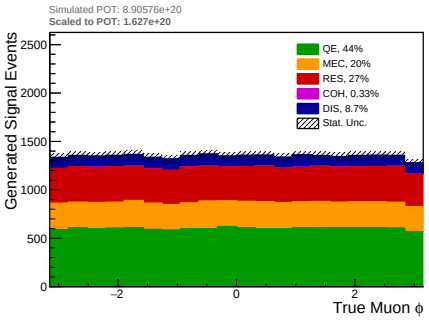

(g) Generated.

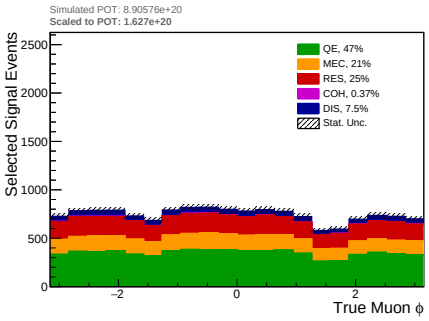

(h) Selected.

Figure 23: Distributions of true variables for generated (left) and selected (right) signal events (ν_μ CC in FV). These plots have been made with a 8.9×10^{20} equivalent POT MC. They have then been scaled to 1.6×10^{20} POT, which are the data POT used for this analysis. The coloured histogram are stacked.

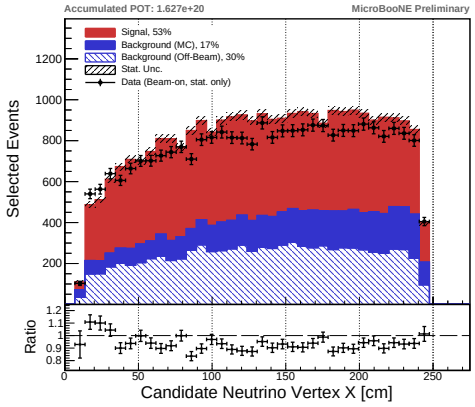

(a) Default GENIE + Emp. MEC.

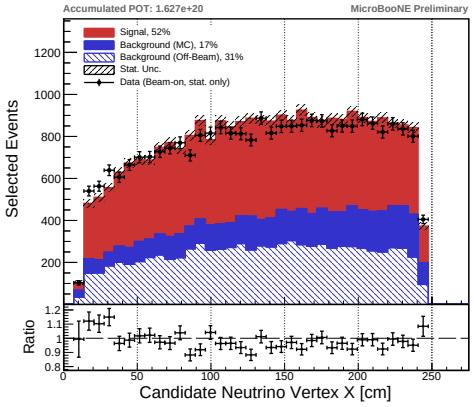

(b) GENIE Alternative.

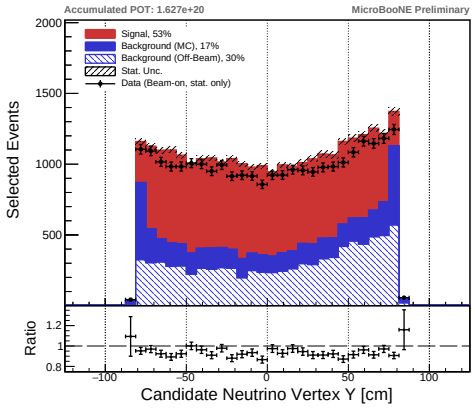

(c) Default GENIE + Emp. MEC.

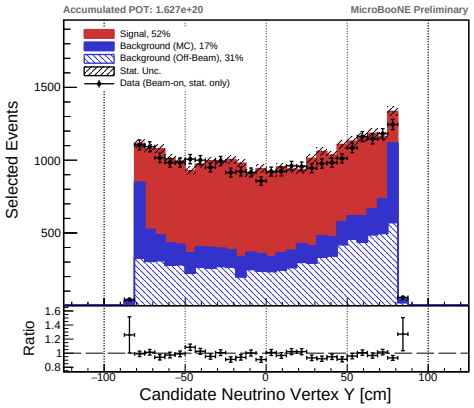

(d) GENIE Alternative.

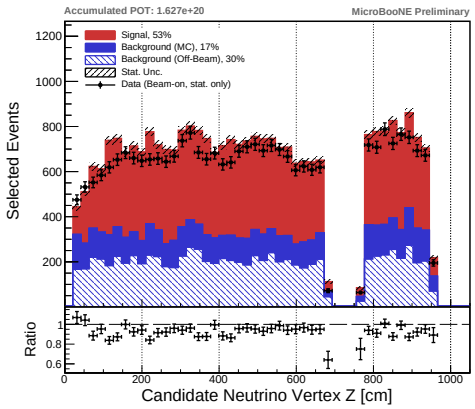

(e) Default GENIE + Emp. MEC.

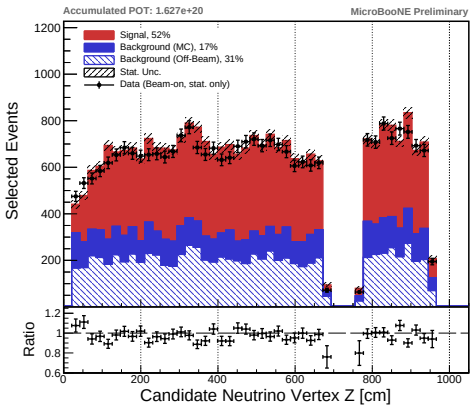

(f) GENIE Alternative.

Figure 24: Final event distributions for the presented selection. The black data points symbolise on-beam data with statistical error bars. The stacked coloured histograms represent the Monte Carlo, with the shaded bands representing the statistical uncertainty only. The two red histograms are the signal events (light red are contained tracks, dark red are un-contained). The shaded histogram is off-beam data. Data and MC correspond to 1.627×10^{20} POT. Left plots show MC from the GENIE default model set, left ones from the alternative one.

References

[1] R. Acciarri et al. "Measurements of Inclusive Muon Neutrino and Antineutrino Charged Current Differential Cross Sections on Argon in the NuMI Antineutrino Beam". In: *Phys. Rev.* D89.11 (2014), p. 112003. DOI: 10.1103/PhysRevD.89.112003. arXiv: 1404.4809 [hep-ex].

[2] C. Anderson et al. "First Measurements of Inclusive Muon Neutrino Charged Current Differential Cross Sections on Argon". In: *Phys. Rev. Lett.* 108 (2012), p. 161802. DOI: 10.1103/PhysRevLett.108.161802. arXiv: 1111.0103 [hep-ex].

[3] K. Abe et al. "Measurement of the muon neutrino inclusive charged-current cross section in the energy range of 1–3 GeV with the T2K INGRID detector". In: *Phys. Rev.* D93.7 (2016), p. 072002. DOI: 10.1103/PhysRevD.93.072002. arXiv: 1509.06940 [hep-ex].

[4] K. Abe et al. "Measurement of the inclusive numu charged current cross section on iron and hydrocarbon in the T2K on-axis neutrino beam". In: *Phys. Rev.* D90.5 (2014), p. 052010. DOI: 10.1103/PhysRevD.90.052010. arXiv: 1407.4256 [hep-ex].

[5] Y. Nakajima et al. "Measurement of inclusive charged current interactions on carbon in a few-GeV neutrino beam". In: *Phys. Rev.* D83 (2011), p. 012005. DOI: 10.1103/PhysRevD.83.012005. arXiv: 1011.2131 [hep-ex].

[6] Q. Wu et al. "A Precise measurement of the muon neutrino-nucleon inclusive charged current cross-section off an isoscalar target in the energy range 2.5 $<$ E(nu) $<$ 40-GeV by NOMAD". In: *Phys. Lett.* B660 (2008), pp. 19–25. DOI: 10.1016/j.physletb.2007.12.027. arXiv: 0711.1183 [hep-ex].

[7] P. Adamson et al. "Neutrino and Antineutrino Inclusive Charged-current Cross Section Measurements with the MINOS Near Detector". In: *Phys. Rev.* D81 (2010), p. 072002. DOI: 10.1103/PhysRevD.81.072002. arXiv: 0910.2201 [hep-ex].

[8] L. Ren et al. "Measurement of the antineutrino to neutrino charged-current interaction cross section ratio in MINERvA". In: *Phys. Rev.* D95.7 (2017), p. 072009. DOI: 10.1103/PhysRevD.95.072009. arXiv: 1701.04857 [hep-ex].

[9] J. Devan et al. "Measurements of the Inclusive Neutrino and Antineutrino Charged Current Cross Sections in MINERvA Using the Low-nu Flux Method". In: *Phys. Rev.* D94.11 (2016), p. 112007. DOI: 10.1103/PhysRevD.94.112007. arXiv: 1610.04746 [hep-ex].

[10] MicroBooNE Collaboration. "Design and Construction of the MicroBooNE Detector". In: *JINST* 12.P02017 (2017). URL: https://arxiv.org/abs/1612.05824.

[11] S. Agostinelli et al. In: *Nucl. Instrum. Methods Phys. Res.* 506.3 (2003), pp. 250–303.

[12] A. A. Aguilar-Arevalo et al. [MiniBooNE Collaboration]. "Neutrino flux prediction at MiniBooNE". In: *Phys. Rev.* D.79 (2009), p. 072002.

[13] The MicroBooNE Collaboration. "Booster Neutrino Flux Predition at MicroBooNE". In: *MICROBOONE-NOTE-1031-PUB* (2018). URL: http://microboone.fnal.gov/public-notes/.

[14] C. Andreopoulos et al. "The GENIE Neutrino Monte Carlo Generator". In: *Nucl. Instrum. Meth.* A.614 (2010), 10.1016/j.nima.2009.12.009.

[15] D. Heck et al. "CORSIKA: A Monte Carlo Code to Simulate Extensive Air Showers". In: *Forschungszentrum Karlsruhe Report FZKA* (1998). URL: https://www.ikp.kit.edu/corsika/70.php.

[16] Ruth Pordes and Erica Snider. In: *PoS ICHEP* 182 (2016). URL: http://inspirehep.net/record/1497601/.

[17] A. Bodek and J. L. Ritchie. "Further studies of fermi motion effects in lepton scattering from nuclear targets". In: *Phys. Rev.* D.24 (1981), p. 1400.

[18] J. Nieves, I. Ruiz Simo, and M. Vicente Vacas. "Inclusive Charged–Current Neutrino–Nucleus Reactions". In: *Phys. Rev.* C.83 (2011), p. 045501. URL: https://arxiv.org/abs/1102.2777.

[19] R. Gran et al. "Neutrino-nucleus quasi-elastic and 2p2h interactions up to 10 GeV". In: *Phys. Rev.* D.88 (2018), p. 113007.

[20] C. H. Llewellyn Smith. "Neutrino reactions at accelerator energies". In: *Phys. Rept.* 3 (1972), p. 261.

[21] T. Katori. "Meson Exchange Current (MEC) Models in Neutrino Interaction Generators". In: *AIP Conf. Proc.* 1663 (2015), p. 030001.

[22] D. Rein and L. M. Sehgal. "Neutrino excitation of baryon resonances and single pion production". In: *Ann. Phys.* 133 (1981), p. 79.

[23] Ch. Berger and L. M. Sehgal. "PCAC and coherent pion production by low energy neutrinos". In: *Phys. Rev.* D.79 (2009), p. 053003.

[24] Costas Andreopoulos et al. "The GENIE Neutrino Monte Carlo Generator: Physics and User Manual". In: *arXiv:1510.05494* FERMILAB-FN-1004-CD (2015).

[25] R. Acciarri et al. "Michel electron reconstruction using cosmic-ray data from the MicroBooNE LArTPC". In: *Journal of Instrumentation* 12.09 (2017), P09014. URL: http://stacks.iop.org/1748-0221/12/i=09/a=P09014.

[26] MicroBooNE Collaboration. "The Pandora multi-algorithm approach to automated pattern recognition of cosmic-ray muon and neutrino events in the MicroBooNE detector". In: *Eur. Phys. J.* C.78 (2018), p. 1. URL: https://arxiv.org/abs/1708.03135.

[27] P. Abratenko et al. In: *JINST* 12.10 (2017), P10010. URL: http://stacks.iop.org/1748-0221/12/i=10/a=P10010.

[28] I. Guyon, B. Boser, and V. Vapnik. "Automatic Capacity Tuning of Very Large VC-dimension Classifiers". In: *Neural Information Processing* (1993). URL: http://citeseerx.ist.psu.edu/viewdoc/summary?doi=10.1.1.17.7215.

[29] The MicroBooNE Collaboration. "Study of Space Charge Effects in MicroBooNE". In: *MicroBooNE Public Note No. 1018* (2016). URL: http://microboone.fnal.gov/public-notes/.

[30] The MicroBooNE Collaboration. "Ionization Electron Signal Processing in Single Phase LAr TPCs I: Algorithm Description and Quantitative Evaluation with MicroBooNE Simulation". In: *submitted to JINST* (2018). URL: https://arxiv.org/abs/1802.08709.

[31] The MicroBooNE Collaboration. "Ionization Electron Signal Processing in Single Phase LAr TPCs II: Data/Simulation Comparison and Performance in MicroBooNE". In: *submitted to JINST* (2018). URL: https://arxiv.org/abs/1804.02583.

[32] Yichen Li et al. "Measurement of Longitudinal Electron Diffusion in Liquid Argon". In: *Nucl. Instrum. Meth.* A816 (2016), pp. 160–170. DOI: 10.1016/j.nima.2016.01.094. arXiv: 1508.07059 [physics.ins-det].

[33] P. Cennini et al. "Performance of a 3-ton liquid argon time projection chamber". In: *Nucl. Instrum. Meth.* A345 (1994), pp. 230–243. DOI: 10.1016/0168-9002(94)90996-2.

[34] V. M. Atrazhev and I. V. Timoshkin. "Transport of electrons in atomic liquids in high electric fields". In: *Trans. Dielectrics and Electrical Insulation* 5 (3 1998), pp. 450–457.

[35] S. E. Derenzo et al. "Test of a Liquid Argon Chamber with 20-Micrometer RMS Resolution". In: *Nucl. Instrum. Meth.* 122 (1974), p. 319.

[36] Eido Shibamura et al. "Ratio of diffusion coefficient to mobility for electrons in liquid argon". In: *Phys. Rev. A* 20 (6 1979), p. 2547.

[37] K. Abe et al. "Measurement of the inclusive numu charged current cross section on carbon in the near detector of the T2K experiment". In: *Phys. Rev.* D87.9 (2013), p. 092003. DOI: 10.1103/PhysRevD.87.092003. arXiv: 1302.4908 [hep-ex].